Atmos. Chem. Phys. Discuss., 14, 2983–3041, 2014
www.atmos-chem-phys-discuss.net/14/2983/2014/
doi:10.5194/acpd-14-2983-2014

Atmospheric Chemistry and Physics Discussions

Constraining mass–diameter relations from hydrometeor images and cloud radar reflectivities in tropical continental and oceanic convective anvils

E. Fontaine[1], **A. Schwarzenboeck**[1], **J. Delanoë**[2], **W. Wobrock**[1], **D. Leroy**[1], **R. Dupuy**[1], **and A. Protat**[2,*]

[1]Université Blaise Pascal, Laboratoire de Météorologie Physique, Aubière, France
[2]Laboratoire Atmosphère, Milieux et Observations Spatiales, UVSQ, Guyancourt, France
[*]now at: Center for Australian Weather and Climate Research, Melbourne, Australia

Received: 9 January 2014 – Accepted: 14 January 2014 – Published: 28 January 2014

Correspondence to: E. Fontaine (e.fontaine@opgc.univ-bpclermont.fr)

Published by Copernicus Publications on behalf of the European Geosciences Union.

Abstract

In this study the density of hydrometeors in tropical clouds is derived from a combined analysis of particle images from 2-D-array probes and associated reflectivities measured with a Doppler cloud radar on the same research aircraft. The mass–diameter $m(D)$ relationship is expressed as a power law with two unknown coefficients (pre-factor, exponent) that need to be constrained from complementary information on hydrometeors, where absolute ice density measurement methods do not apply. Here, at first an extended theoretical study of numerous hydrometeor shapes simulated in 3-D and arbitrarily projected on a 2-D plane allowed to constrain the temporal evolution of the exponent of the mass–diameter relationship with that of the exponent of the surface–diameter relationship that is measured by the 2-D-array probes. The pre-factor is then constrained from theoretical simulations of the radar reflectivities matching the measured reflectivities along the aircraft trajectory.

The study has been performed as part of the Megha-Tropiques satellite project, where two types of mesoscale convective systems (MCS) have been investigated: (i) above the African Continent and (ii) above the Indian Ocean. In general, both mass-diameter coefficients (pre-factor and exponent) decrease with decreasing temperature, the decrease is more pronounced for oceanic MCS. The condensed water contents (CWC) calculated from particle size distributions (PSD) and $m(D)$ also decrease with altitude while the concentrations of the hydrometeors increase with altitude. The calculated values of CWC are largest for continental MCS.

1 Introduction

The French–Indian satellite Megha-Tropiques, launched in 2011, is primarily devoted to improve our knowledge on the understanding of the water cycle processes in the tropical troposphere. In particular, the satellite allows studying the life cycle of tropical convective systems over ocean and continents, the environmental conditions for their

ACPD
14, 2983–3041, 2014

formation and evolution, their water budget, and the associated water vapor transport. The overall purpose of our study is to improve the surface rain rate retrieval calculated with the BRAIN algorithm (Viltard et al., 2006) from brightness temperatures measured on the satellite. The most relevant instrument on the satellite for cloud studies is the MADRAS microwave imager with 9 frequencies (18.7 to 157 GHz). One of the major sources of errors in deriving rainfall rates from the brightness temperatures is the lack of knowledge about the density of the complex shaped atmospheric ice particles. Within the Megha-Tropiques project, two measurement campaigns (presented in more detail in Sect. 2) have been conducted in order to get a better statistical description of the microphysical properties of hydrometeors and finally, to improve the rain rate retrieval from the Megha-Tropiques satellite but also from similar satellites measurements, like TRMM (tropical rainfall measurement mission, Huffman et al., 2007) or SSM/I (Special Sensor Microwave/Imager, Spencer et al., 1989).

The main focus of this study is more precisely to characterize the statistical relationship between the mass and maximum diameter $m(D)$ of ice crystals by developing a retrieval technique that combines radar reflectivity and particle imagery in order to produce reliable calculations of the condensed water content (CWC). A series of earlier studies already related cloud radar reflectivity (usually at a frequency of 94 GHz) and in-situ measurements of cloud microphysical properties. However, the variability of the ice crystal density in space and time has been rarely examined. For instance in Protat et al. (2007), Hogan et al. (2006), and Pokharel and Vali (2011) the condensed water content is calculated assuming a constant mass–size relationships for all clouds.

The most usual empirical expression used to predict the mass for various types of ice crystals shapes (Locatelli and Hobbs, 1974; Mitchell, 1996, hereafter M96; Heymsfield and Westbrook, 2010; McFarquhar et al., 2007) is formulated as a power law which is usually a function of the maximum length (hereafter D_{max}), or the mean diameter (average of the maximum length in the y axis and the maximum value of x axis; Brown and Francis, 1995, hereafter BF95) of the 2-D hydrometeor images.

ACPD
14, 2983–3041, 2014

In this paper the mass m (in gram) is presented as a power law function of D_{max} (in centimeters):

$$m(D_{max}) = \alpha \cdot D_{max}^{\beta} \quad (1)$$

In other studies the mass (and thus density) of hydrometeors has been determined following various principles. For example, ice crystals have been collected on a sheet of plastic or a Petri dish. After taking microphotographs of the crystals, these have been melted to deduce their mass from the resulting hemispherical drops (Locatelli and Hobbs, 1974; Mitchell et al., 1990). Another method used is to classify hydrometeors according to their crystal habits associated to specific $m(D)$ relations for individual habits, following the scheme given by Magono and Lee (1966). Furthermore, when the CWC mass concentration is measured directly and simultaneously from the 2-D images of hydrometeors, $m(D)$ relations can be derived from integral CWC data and corresponding particle size distributions (hereafter PSD) extracted from the images. BF95 used simultaneously a Lyman-α absorption hygrometer (Nicholls et al., 1990) and a 2-D Optical Array Probe (OAP) to determine coefficients α and β for cirrus clouds. Heymsfield et al. (2002) developed an expression of the crystal mass as a function of D_{max} and the area ratio A_r (the projected area of an ice particle normalized by the area of a disc having the same D_{max}) for bullet-rosettes present in cirrus clouds. This approach was confronted with real measurements of CWC measured with a Counterflow Virtual Impactor (Ogren et al., 1985) and corresponding 2-D images (OAP 2-DC and 2-DP) in cirrus clouds from airborne measurements. A detailed description of the particle habits which is needed for the previous approach was provided by the high resolution 2-D images from the Cloud Particle Imager CPI (Lawson et al., 1998). Retrieved $m(D)$ relationships are finally used to compute Ka-band radar equivalent reflectivities, which are in good agreement with measured reflectivities.

Baker and Lawson (2006) introduced a new scheme which is a combination of fundamentals geometric parameters (perimeter, width, D_{max} and projected area) of the 2-D images to deduce the mass of individual particles. This method was validated against

ACPD
14, 2983–3041, 2014

the dataset of Mitchell et al. (1990) and has the advantage of not requiring particle habit assumptions. McFarquhar et al. (2007) derived $m(D)$ relationships from vertical profiles in the stratiform part of Mesoscale Convective Systems (hereafter MCS) above the North American continents within and below the melting layer. α and β coefficients were calculated from measured reflectivities and PSD deduced from the OAP 2-DC and 2-DP probes. With the improvement of the numerical simulations, Schmitt and Heymsfield (2010, hereafter SH2010) have simulated the aggregation of plates or columns. Fractal 2-D and 3-D analyses of these aggregates allowed them to derive a relationship to calculate the exponent β from the 2-D images. Once β has been fixed, these results were confronted with aircraft in situ data from CRYSTAL-FACE (Cirrus Regional Study of Tropical Anvils and Cirrus Layers–Florida Area Cirrus Experiment) and remote sensing data from ARM (Atmospheric Radiation Measurement) project in March 2000, which finally allowed to estimate dependencies of α and β as a function of temperature Heymsfield et al. (2010, herafter H10) demonstrate that a strong relationship exists between α and β coefficients and argue that the BF95 relationship overestimates the prefactor α for stratiform clouds, whereas α is underestimated for convective clouds.

In our study, CWC was not measured directly in one of the two experiments. In order to calculate CWC, cloud ice density of hydrometeors needs to be derived from joint analysis of the radar reflectivity measured by the 94 GHz cloud radar RASTA (Protat et al., 2009), and cloud particle images measured simultaneously with 2-D array probes on the same aircraft. The α and β coefficients are constrained from particle imagery and from theoretical simulations of crystal images, combined with subsequent simulations of cloud reflectivities compared to measured ones. In the following section the two Megha-Tropiques aircraft measurement campaigns and corresponding in-situ microphysical measurements are described. A general technique for the retrieval of CWC is presented in Sect. 3. Then theoretical simulations of 3-D crystal shapes and associated results are presented in a fourth section, while the fifth section presents a sensitivity study of the parameterizations of β from real particle images and there effects on $m(D)$ relationships.

ACPD
14, 2983–3041, 2014

2 Cloud data from the Megha-Tropiques flight campaigns

Two airborne measurement campaigns have been conducted with the French Falcon 20 research aircraft from SAFIRE (Service des Avions Français Instrumentés pour la Recherche en Environnement). During the first campaign, The Falcon20 has been flown out from Niamey (Niger), in August 2010 (hereafter MT2010) during the monsoon season above the West African continent. The second campaign has been conducted above the Indian Ocean between November and December 2011 (hereafter MT2011) at Gan (Maldives). A brief description of the research flights and sampled convective cloud systems selected for this study is presented in Table 1. Cloud systems observed during MT2010 were typically MCS, with most of the flights performed in the stratiform part of these MCS within the temperature range down to −35 °C. During MT2011, two types of systems were observed: in the first part of the campaign two MCS systems were sampled, whereas in the second part the convection has been much less organized and only more isolated smaller systems have been encountered.

The Falcon 20 has been equipped with active remote sensing and cloud microphysics in situ instrumentation. Next to the Doppler cloud radar RASTA (Protat et al., 2009) in-situ measurements of microphysical properties were performed using a new generation of Optical Array Probes (OAP): the 2-D Stereo probe (2-DS) from Stratton Park Engineering Company (SPEC) Inc. and the Precipitation Imaging Probe (PIP) from Droplet Measurement Technologies (DMT). In addition, during MT2011 a Nevzorov probe (Korolev et al., 1998) has been installed on the Falcon20 to measure CWC.

In order to derive particle size distributions and aspect ratios from the 2-D images, standard corrections of the OAP data have been performed. In particular, rejection of 2-D images due to shattering (Field et al., 2006; Korolev and Isaac, 2005) and also rejection of splashes have been applied. Moreover, reconstruction of truncated images which are partially recorded has been employed (Heymsfield and Parrish, 1978). Finally, the pixel resolution (10 µm for the 2-DS, 100 µm for the PIP) is corrected for the

ACPD
14, 2983–3041, 2014

true air speed (Baumgardner and Korolev, 1997), in order to account for the fixed speed setting during data acquisition.

2-D images recorded with 2-DS and PIP probes were processed using the software developed at LaMP (Laboratoire de Météorologie Physique) for CPI images (Lefèvre, 2007) and improved for black and white 2-D images in order to extract a large variety of geometrical parameters, such as maximum diameter D_{max}, width perpendicular to D_{max} direction, projected area (hereafter Sp), and perimeter. Then for each probe, the number particle size distribution (PSD) and the mean aspect ratio distribution (hereafter AsD) are calculated as a function of D_{max} L^{-1} μm^{-1}. With these distributions we build composite distributions for PSD and AsD from both probes. The size range of these distributions spans from 50 to 6450 microns in D_{max}. Equations (2) and (3) describe the simple interpolation scheme used to build the composite number PSD distributions, an analogue scheme is used to derive AsD composite distributions.

$$\sum_{D_{max}=50}^{D_{max}<6450} N(D_{max})\cdot\Delta D_{max} = \sum_{D_{max}=50}^{D_{max}<450} N_{2DS}(D_{max})\cdot\Delta D_{max} + C_1(D_{max})\cdot\sum_{D_{max}=450}^{D_{max}<950} N_{2DS}(D_{max})\cdot\Delta D_{max} + C_2(D_{max})\cdot\sum_{D_{max}=450}^{D_{max}<950} N_{PIP}(D_{max})\cdot\Delta D_{max} + \sum_{D_{max}=950}^{D_{max}<6450} N_{PIP}(D_{max})\cdot\Delta D_{max} \quad (2)$$

with

$$C_1(D_{max}) + C_2(D_{max}) = 1; \quad \text{and} \quad C_2(D_{max}) = (D_{max} - 450)/(950 - 450) \quad (3)$$

ACPD
14, 2983–3041, 2014

These composite distributions are mainly composed of three parts. The first part, which comprises the size range of 50–450 microns, is made of pure 2-DS distributions (N_{2DS}), whereas the third part between 950–6400 microns is purely taken from PIP (N_{PIP}) distributions. The intermediate second part is obtained by weighting the 2-DS and PIP distributions with a transfer function (Eq. 3) which increases the weight of the PIP and decreases the weight of the 2-DS data with increasing D_{max}. The bin resolution of the composite distributions is given by ΔD_{max} equal to 10 microns and the spectra are averaged over time steps of 5 s. Examples of PSD and TSD are presented in Fig. 1. Overall the 2 probes are in good agreement in their common size range. Figure 1a shows the PSD composite distribution and the individual PSDs of the individual probes. The AsD composite distribution is shown in Fig. 1b. It can be seen that the transfer function smoothes the transition from the 2-DS to the PIP.

3 CWC retrieval

In order to better understand the importance of the coefficients α and β in Eq. (1) for the retrieved CWC simulations of reflectivity at 94 GHz have been performed and compared with the measured ones. Simulations of radar reflectivity are complex when considering non-spherical ice crystals. In this study, the backscatter properties of the hydrometeors have been simulated with the T-matrix method (Mishchenko et al., 1996) for crystals and/or with Mie theory for spherical properties. In order to model the scattering properties of the ice particles, these particles are assumed to be oblate spheroids with a flattening that equals the mean aspect ratio $\overline{\mathrm{As}}$ of all the hydrometeors recorded in the 5 s time step:

$$\overline{\mathrm{As}} = \frac{\sum_{D_{max}} N(D_{max}) \cdot \mathrm{As}(D_{max})}{\sum_{D_{max}} N(D_{max})}, \quad (4)$$

where $N(D_{max})$ is the concentration of the hydrometeors and $\mathrm{As}(D_{max})$ their average aspect ratio. Figure 2, shows the impact of As on the effective reflectivity for 94 GHz,

ACPD
14, 2983–3041, 2014

for varying As between 0.5 and 1. For As = 1 Mie theory was applied. For diameters less than 600–900 µm simulated radar reflectivities agree well with those calculated using the Rayleigh approximation. As can be seen in this figure, the so-called "Mie effects" appear only for larger diameters and decreasing aspect ratio As.

In general, we assume that hydrometeors consist of a homogeneous mixture of ice and/or air. Their dielectric properties of the particles are therefore a function of the mass–diameter relationship that represents the fraction of ice f_{ice} (Eq. 5) in the hydrometeors. Equation (5) explains how the ice fraction of the solid hydrometeor are calculated, with $\rho_{ice} = 0.917\,g\,cm^{-3}$. The ice fraction f_{ice} cannot exceed 1.

$$f_{ice} = \min\left(1, \frac{\alpha \cdot D_{max}^{\beta}}{\frac{\pi}{6} \cdot \rho_{ice} \cdot D_{max}^{3}}\right). \quad (5)$$

Once f_{ice} is determined the refractive index is calculated using the approximation of Maxwell Garnet (1904). The mass of the spheroid does not depend on the aspect ratio As, but the backscattering properties do. By means of the T-matrix method the backscattering coefficient of a particle is calculated assuming the particle volume as a prolate spheroid with a diameter $D_{Tmatrix}$:

$$D_{Tmatrix} = D_{max} \cdot \sqrt[3]{\frac{1}{As}} \quad (6)$$

In order to calculate the 94 GHz radar reflectivity, the particle number distribution $N(D_{max})$, its mean aspect ratio As, and the ice fraction f_{ice} of the hydrometeors, also the coefficients α and β of the mass–diameter relation (Eq. 1) must be given. Figure 3 gives an outline of the technique developed to retrieved the $m(D)$ coefficients. After imposing a fixed value β_i the prefactor α (hereafter called α_i) is determined by minimizing the difference between the simulated and measured reflectivities. RASTA reflectivity along the flight trajectory has been calculated using a linear interpolation between the closest reflectivities above and below the aircraft (typically at 300 m range from the aircraft).

ACPD
14, 2983–3041, 2014

The reflectivity simulations were performed for β_i coefficients in the interval [1,3] with a step of 0.01. With this set of 201 (α_i, β_i) solutions, the corresponding values for CWC(α_i, β_i) in (g m^{-3}) were calculated:

$$\mathrm{CWC}(\alpha_i,\beta_i) = 10^3 \cdot \sum_{D_{\max}=50\,\mu\mathrm{m}}^{D_{\max}=6400\,\mu\mathrm{m}} N(D_{\max}) \cdot \alpha_i D_{\max}^{\beta_i} \cdot \Delta D_{\max}. \quad (7)$$

Figure 4 shows an example of the retrievals for the flight number 18 of MT2010. In Fig. 4a the concentration of the hydrometeors is shown as a function of flight time and hydrometeor size. In addition, the radar reflectivity is added on a right y axis (black curve). Figure 4b shows solutions for α_i (see color legend) as a function of the imposed β_i value (see y axis). Figure 4c depicts the time evolution of all 201 curves of CWC which were calculated from the coefficients α_i and β_i, using Eq. (7). Although the spread of both coefficients, as illustrated in Fig. 4b, is fairly large, the ensemble of CWC values for a given time remains well within the same order of magnitude. Maximum differences of ±2 g m^{-3} are found for very high CWC (e.g. at 13:45 UTC), but for most other times the spread between the calculated CWC(α_i, β_i) values is less than 30 %.

In order to better quantify the uncertainty in CWC resulting from the multiple possible couples α_i,β_i the following error analysis was performed:

An average value $\overline{\mathrm{CWC}(\alpha_i,\beta_i)}$ is calculated from the set of CWC:

$$\overline{\mathrm{CWC}(\alpha_i,\beta_i)} = \frac{1}{N_{\mathrm{tot}}} \sum_{\beta_i=1}^{\beta_i=3} \mathrm{CWC}(\alpha_i,\beta_i), \quad (8)$$

where $\overline{\mathrm{CWC}(\alpha_i,\beta_i)}$ is given in g m^{-3} and N_{tot} is the number of (α_i, β_i) solutions (with $N_{\mathrm{tot}} = 201$).

We then define the maximum uncertainty ($\Delta\mathrm{CWC}_{\max}$) of the retrieved CWC as the maximum difference between the average value of all calculated CWC (for all solutions

ACPD
14, 2983–3041, 2014

(α_i,β_i)) and the largest or smallest value of CWC for a given time. More precisely this maximum uncertainty is calculated in terms of the relative error in percent:

$$\Delta\mathrm{CWC}_{\max} = 100\frac{\mathrm{MAX}(|\mathrm{CWC}(\alpha_i,\beta_i) - \overline{\mathrm{CWC}(\alpha_i,\beta_i)}|)}{\overline{\mathrm{CWC}(\alpha_i,\beta_i)}}. \quad (9)$$

For both measurement campaigns MT2010 and MT2011, Fig. 5 shows the distribution of $\Delta\mathrm{CWC}_{\max}$ in percent. For most of the calculated CWC values the maximum errors remain below 30 %. Average values of the maximum deviations in CWC are 21 % for MT2010 and 20 % for MT2011, respectively.

These uncertainties do not take into account the uncertainty related to the measurements of the reflectivity by the cloud radar RASTA. Table 2 gives the impact of the reflectivity on the retrieved $m(D)$ coefficient α. For example, if the reflectivity is shifted by +1 dBZ to simulate a radar calibration error, the CWC retrieval is increased by 11 % with respect to the CWC given by the measured reflectivity. Furthermore, we tried to quantify the impact of the $\overline{\mathrm{As}}$ on the retrieved CWC, we estimate that for a shift of +10 % of the flattening parameter, CWC increases by 6 % (Table 3). The CWC retrieval of this method is pretty sensitive to uncertainties in measured reflectivities and also to the shape (or flattening) parameter used to simulate the radar reflectivity.

In fact, Fig. 4b shows that it exists an infinity of solutions (α_i, β_i) which allows simulating the measured reflectivity at a given time. If we would impose that one of the two coefficients α or β stays constant during the flight, this does not imply that the other coefficient will also stay constant. This demonstrates clearly that the spatiotemporal variability of the microphysical properties of an MCS cannot be well represented by a constant $m(D)$ relationship. Thus, allowing variations of the $m(D)$ relationship in time still does not resolve the problem of deriving the best solution among all the possible solutions (α_i, β_i). Further information from hydrometeor images is therefore used in the next section to constrain β before running the reflectivity simulations in order to reduce the number of unknowns down to one (the pre-factor α).

ACPD
14, 2983–3041, 2014

4 Study of 2-D and 3-D aspects of hydrometeor images

4.1 Surface–diameter relationships of natural hydrometeors

This section focuses on the surface–diameter relationship (hereafter $S(D)$; Eq. 10) and also on the correlation which exists between D_{max}, projected area Sp and the mass of hydrometeors.

$$S(D_{max}) = \gamma D_{max}^{\sigma} \quad (10)$$

Since ice crystals have complex and varied shapes, the description of their volume (or mass) and their projected area Sp onto a 2-D plane as a function of the particle diameter cannot be described unambiguously with constant exponents σ (for $S(D)$) or β (for $m(D)$). The work presented here is inspired by a study of Schmitt and Heymsfield (2010) who improved the parameterization of $m(D)$ relationships applying a fractal analysis on aggregated ice crystals.

$S(D)$ relationships are calculated by fitting the projected surface of the hydrometeors as a function of their D_{max}, thereby using a power law as described in Eq. (10). Measurements of the projected surfaces are provided by the 2-DS and PIP in-situ microphysical probes. The calculation of a single $S(D)$ relationship is difficult using both probes since in their common size range the pixel resolution of both instruments differs significantly (by a factor 10). This impacts parameters such as the particle length or width (which allow us to build composite distribution for this kind of parameters) to some extent, but the projected surface to a larger extent. Therefore in this study $S(D)$ is calculated from the 2-DS probe only, since using the $S(D)$ of the PIP would not make sense for sub-millimetric particles (1 mm length corresponds to 10 pixels), where the 2-DS offers higher resolution images. Thus, by using the images of the 2-DS probe the $S(D)$ relationship is calculated along the flight trajectory with a constant time resolution of 5 s.

ACPD
14, 2983–3041, 2014

4.2 Simulations of artificial ice crystals shape and associated $S(D)$ and $m(D)$

Optical array probes (OAP) measure the shadow projection of randomly oriented 3-D cloud particles on a 2-D plane. Theoretical simulations of 3-D crystals are described in more detail in Appendix A. The corresponding 2-D projections are based on the same principle of randomly oriented 3-D particles projected on a 2-D plane. These 2-D images are processed with the same algorithm used for real particle images in order to deduce particle projected area Sp and maximum diameter D_{max} of each random projection. Overall, 30 different kind of hydrometeors have been simulated and tested. Figure 6 shows some examples of arbitrarily oriented 3-D crystals (stellar, columns, plates, capped-columns and rosettes) that have been projected onto a plane. As for the 2-DS probe, a pixel resolution of 10 µm has been chosen. The simulations explore the effects of different types of crystal shapes and of different sizes of distinct shapes on the statistical $S(D)$ and $m(D)$ relationships. Power law exponents σ for $S(D)$ and β for $m(D)$ have been calculated for all 30 individually tested particle types and are shown in Fig. 7 and reported in Table 4. In order to compare with existing values of σ and β found in the literature, we have added the values given in M96. In addition, Table 4 summarizes the values and the associated symbols of each individual simulated particle shape. In order to correlate the exponent β of the $m(D)$ relation to the exponent σ of the $S(D)$ relation, all data points resulting from the 30 simulations presented here are fitted by a linear function (Eq. 11). The fitted function $\beta(\sigma)$ is valid for σ between 1 and 2, thus yielding values for β in the range [0.95;2.99].

$$\beta(\sigma) = 2.3\sigma - 1.7 \tag{11}$$

From the obtained results one can notice that varying the linear ratio between H and L for plates (also valid for slender stellars, solid stellars, and rosettes) does not impact significantly σ and β, whereas a nonlinear ratio $H = \sqrt{L}$ has more impact on both exponents. The latter case produces results closer to measurements presented by M96 (Table 2), with simulations from our study resulting in $\sigma = 1.80$ and $\beta = 2.49$ and

ACPD
14, 2983–3041, 2014

M96 measurements resulting in $\sigma = 1.85$ ($D_{max} < 100\,\mu m$) and $\beta = 2.45$, respectively. For $D_{max} > 100\,\mu m$, results are not readily comparable with the M96 results as in their study random orientation is not assumed. Regarding columns, an increase of the ratio H/L has more impact on σ and β. As stated for hexagonal plates, also for columns the nonlinear ratio $L = \sqrt{H}$ brings the simulations closer to the M96 measurements, with $\sigma = 1.49$ and $\beta = 1.75$ for simulations (this study) and $\sigma = 1.41$ and $\beta = 1.74$ for the M96 measurements. Other habits from the M96 measurements are not comparable to our simulations.

In view of the results produced by the 3-D simulations, it seems that β (and also σ) does not relate much to the sphericity of the crystal shape, but more to how a population of ice crystals is growing in the 3-D space (axis x, y, z). The behavior of the exponent β for plates and stellars but also for rosettes shows that, if the crystal height grows at the same speed as the length (which is a combination of the growth on 2 axis), then β is close to 3. In contrast, if the growth in length is two times larger than the height, then β is closer to 2.5. Finally, if the height stays constant while the length is growing, then β gets close to 2.

5 Mass–diameter relationship

This part is focusing on the particular solution for $m(D)$, where we relate the exponent σ of the $S(D)$ relation to the exponent β of the $m(D)$ relation. After the analysis of the particle surfaces $S(D_{max})$ given by the 2-D images of the OAP probes the coefficients σ and γ (see Eq. 10) are determined by a power law fit. Once σ is calculated, the exponent β can be calculated from Eq. (11) and this particular solution for β is called hereafter β_σ. The remaining coefficient α of the $m(D)$ relationship (Eq. 1) is finally determined by means of the observed 94 GHz reflectivity according to the retrieval technique presented in Fig. 3. Then, $m(D)$ is strongly related to the 2-D images recorded by the OAP probes and the retrieved couple (α_σ, β_σ) is chosen such that β_σ is resulting from Eq. (11) as a function of flight time.

ACPD
14, 2983–3041, 2014

Subsequently, CWC(α_σ,β_σ) is calculated from Eq. (7) for the couple (α_σ,β_σ) of the $m(D)$ relationship. Figure 8 shows the temporal evolution of the PSD, aspect ratio $\overline{As}$, exponent β_σ, derived α_σ, and calculated CWC(α_σ, β_σ) for a cloud sequence of the flight 18 during MT2010.

CWC(α_σ,β_σ) is compared with the B&L (Baker and Lawson, 2006) scheme computing $CWC_{B\&L}$ from the 2-D images. This method was chosen among others because it does not make any assumption on particle habit and calculates the condensed mass particle by particle. Figure 9 shows calculated CWC(α_σ,β_σ) vs. $CWC_{B\&L}$. The two CWC estimates are fitted using a power law. The exponent found is close to 1 which indicates we are close to the linearity between the two calculations for the two campaigns: 1.06 for MT2010 (Fig. 9a) and 1.01 for MT2011 (Fig. 9b). For MT2010 CWC(α_σ,β_σ) is 70 % larger than $CWC_{L\&B}$, whereas for MT2011 CWC(α_σ,β_σ) is larger than $CWC_{L\&B}$ by about 50 %. Of course the data set of hydrometeors coming from winter storms in the central Sierra Nevada and collected at the ground, which was fitted to build the B&L scheme is not necessarily best adapted for the hydrometeor data set used in our study. Comparisons between the two CWC retrieval methods also exhibit good correlation coefficients of 0.93 for MT2010 and 0.92 for MT2011, respectively. However, strong deviations in the absolute values of calculated CWCs persist. In addition, error bars for all analyzed CWC are given in Fig. 9 presenting their minimum and the maximum values which were determined by the retrieval technique for (α_i, β_i) presented in Sect. 3. Comparisons of CWC(α_σ,β_σ) vs. CWC measured by the Nevzorov (hereafter $CWC_{Nevzorov}$) probe are also shown in Fig. 9c. A very good agreement is reached for values in the range $[0.1;1.4]\,g\,m^{-3}$ (Fig. 9c). CWCs are in the same order and the correlation coefficient is equal to 0.93. Uncertainties on the retrieved CWC(α_σ, β_σ) (e.g. Sect. 3) and also $CWC_{Nevzorov}$ are somewhat larger for small CWC values. For $CWC_{Nevzorov}$ the uncertainty is particularly related to the calculation of the Nevzorov probe dry power. As a consequence the correlation coefficient decreases (0.9) when taking into account CWC values below $0.1\,g\,m^{-3}$. Moreover, in the unattended version of the Nevzorov probe we cannot oppress the offset during data acquisition, which

ACPD
14, 2983–3041, 2014

means that the probe saturates far below the nominally possible $3\,g\,m^{-3}$. Therefore, CWC saturation threshold has been taken into account as a function of calculated Nevzorov probe offset during flight conditions. Beyond that threshold of roughly $1.4\,g\,m^{-3}$, CWC(α_σ,β_σ) and $CWC_{Nevzorov}$ cannot be compared.

The two $m(D)$ coefficients (α_σ,β_σ) appear to be strongly correlated with each other, with a correlation coefficient (cc) that equals 0.81 for MT2010 (Fig. 10a) and 0.92 for MT2011 (Fig. 10b). This type of results has already been found and discussed in H10. Their dataset was divided into two types of cirrus: convective cirrus and stratiform cirrus. H10 obtained trends for each type of cirrus by fitting the mean of the prefactor (here α), as a function of the exponent (here β). In Fig. 10, the power law fit obtained for convective cirrus by H10 is added as a black line. We note in the semi-log representations of Fig. 10 that the slope derived by H10 is exceeding the slopes calculated for MT2010 and MT2011, respectively. This may be explained by the calculation of the β coefficients in H10 which is different from this study.

Furthermore, Fig. 10 reveals that temperature has an impact on the relationship between α_σ and β_σ, which was not discussed in H10. In particular, for a given exponent β_σ the prefactor α_σ increases with increasing temperature.

In order to account for this temperature dependence of the α_σ–β_σ relationship, two parameterizations are proposed for continental (MT2010) and oceanic MCS (MT2011) data, respectively. Equation (12) presents the two relationships between α_σ, β_σ and T in [K], where the first part of the equation illustrates the impact of the temperature and the second part of the equation the influence of β coefficient of the crystals.

$$\left.\begin{aligned} \text{MT2010: } \alpha_\sigma &= (0.0194 \cdot T - 3.9093) \cdot e^{-9.15} \cdot e^{2.16 \cdot \beta_\sigma} \\ \text{MT2011: } \alpha_\sigma &= (0.0139 \cdot T - 2.5854) \cdot e^{-10.51} \cdot e^{2.68 \cdot \beta_\sigma} \end{aligned}\right\} \quad (12)$$

Our dataset also offers the opportunity to gain further insights into the continental vs. oceanic variability of cloud parameters. Figure 11a–f shows vertical variations of various cloud parameters such as α_σ, β_σ, $N_T = (\sum N(D_{max})\Delta D_{max})$, Z_{RASTA}, and CWC(α_σ,β_σ) for the two types of tropical convective systems (MT2010 and MT2011,

ACPD
14, 2983–3041, 2014

respectively). The vertical variation of these parameters is presented as a function of temperature. The calculated profiles for MT2011data include solely the flights 45 and 46 in a well developed stratiform region of an extended convective system. Averages have been calculated for temperature intervals of 5 K. Figure 11a indicates the number of observations (i.e. 5 s average data points) taken into account to deduce the average value for the corresponding temperature interval. The number of observations is smaller for MT2011 relative to MT2010. The two data points for MT2011 for lowest temperatures (240 K and below) have been calculated only from a few measurements. Also values given in the melting layer (points at 275 K and 280 K) also need to be treated with caution, since our retrieval method does not take into account the liquid water at the surface of melting ice crystals.

Standard deviations are shown by the error bars, and represent the horizontal variability for measured and retrieved parameters. Figure 11b illustrates the trend of β_σ, which shows a small decrease with altitude for MT2010. For MT2011, the decrease of β_σ with temperature is more pronounced in the upper altitudes (temperatures below 260 K), but with an eventual increase in the lower altitudes (beyond 260 K). However, the horizontal variability of β_σ coefficients is larger for MT2011. MCS systems sampled over West Africa were typically squall lines, those systems are composed by a convective part in the front of the systems and a trailing stratiform part. MCS encountered over the Indian Ocean were part of the Inter Tropical Convergence Zone and were not as organized as the continental MCS. Therefore microphysical processes seem to be more heterogeneous in the stratiform part of oceanic MCS as compared to the stratiform part of continental MCS over West Africa. In addition, our results are compared with data from another study on cirrus tropical convective clouds (SH2010). Exponents proposed in SH2010 are smaller and their decrease is more pronounced than for MT2011 and MT2010. As SH2010 give the vertical profile of $m(D)$ coefficients as a function of the temperature, it is worthwhile to compare the three profiles of $m(D)$ coefficients available for tropical clouds. In Fig. 11c, the pre-factors α for SH2010 are smaller than those found for MT2010 and MT2011. In general, α decreases with altitude for both

ACPD
14, 2983–3041, 2014

campaigns MT2010 and MT2011 and between 265 K and 245 K, the vertical trends of α for MT2010 and MT2011 are similar. Figure 12d shows an increase of the total number concentration of hydrometeors with decreasing temperature, with a larger number concentration of hydrometeors encountered during MT2010 as compared to MT2011.

Figure 11e demonstrates that RASTA radar reflectivities decrease with temperature and are larger for MT2010 than for MT2011. Below 260 K the horizontal variability of Z_{RASTA} is increasing, especially in the oceanic stratiform conditions (MT2011). Similar to the reflectivity profile also the CWC decreases with altitude. This decrease with height is most pronounced for the observation under oceanic conditions during MT2011 (Fig. 11f). Comparing the stratiform regions of MCS systems between MT2010 (continental conditions) and MT2011 variations in the partitioning of CWC with altitude may indicate different efficiencies of the aggregation process in oceanic and continental anvils, but may also be caused by the smaller number of samples taken in the uppermost levels, especially during MT2011. Figure 12 then provides average vertical profiles of microphysical parameters (PSD, effective particle density, mass and calculated reflectivity at 94 GHz) as a function of particle diameter. Figure 12a and b shows average PSDs for the entire size range measured with the 2-DS and PIP probes. For MT2010 the smallest ($< 70\,\mu$m) and the largest particles sizes ($> 500\,\mu$m) stay quite constant in number along the vertical, whereas the medium sized hydrometeors for which the particle growth is dominated by water vapor diffusion (in the range from 150–400 microns) increase in number with altitude. For MT2011 the concentrations of the smallest and largest hydrometeors decrease slightly with altitude, while the number of medium sized hydrometeors (200–400 microns) increases with altitude, as already discussed for MT2010. Figure 12c and d shows the effective density of cloud particles when hydrometeors are considered as spheres with the equivalent diameter D_{max}. Since ice particles are considered in this paper as a homogeneous mixture of ice and air their effective density ρ_{eff} can be determined by Eq. (13), reflecting the fact that this

ACPD
14, 2983–3041, 2014

value cannot exceed the density of pure ice (0.917 g cm^{-3})

$$\rho_{\text{eff}}(D_{\text{max}}) = \min\left(0.917, \frac{6 \cdot \alpha_\sigma}{\pi} \cdot D_{\text{max}}^{\beta_\sigma - 3}\right). \quad (13)$$

As $\rho_{\text{eff}}(D_{\text{max}})$ is a function of α_σ and β_σ, the density behavior comprises the impact of the temperature on the $m(D)$ coefficients. In general, for MT2010, the effective density (Fig. 12c) continuously decreases with decreasing temperature, while this decrease is less pronounced for MT2011 (Fig. 12d). The particle effective density increase for small sizes. This observational result may be due to low number of samples available in the high altitude during MT2011. Figure 12e and f shows the partitioning of the total mass $M(D_{\text{max}})$ in g m^{-3} µm^{-1} for a given D_{max} calculated as follows from the individual crystal images:

$$M(D_{\text{max}}) = 1000 \cdot N(D_{\text{max}}) \cdot \alpha_\sigma D_{\text{max}}^{\beta_\sigma}. \quad (14)$$

For temperatures from 260–270 K most of the total mass resides in the range 200 µm < D_{max} < 3 mm. At these temperatures the impact of particles smaller than 200 microns is not important. However, for colder temperatures much more of the ice mass is contained in smaller particles, for example for temperature below 240 K the mass resides mainly in the range from 200 to 700 µm. This vertical gradient is shifted to smaller particle sizes and is slightly more pronounced for MT2011, where for temperatures less than 240 K the mass resides in the range 200 µm < D_{max} < 500 µm.

In Fig. 12g and h, we can see the simulated backscattering properties of the hydrometeors at 94 GHz as a function of D_{max} and temperature. At this frequency the major response of the reflectivity stems from hydrometeors in the size range of 0.2–2 mm, for MT2010 (Fig. 12g), and 0.3–2 mm for MT2011 (Fig. 12h), respectively. MT2011 reflectivity shows a more pronounced decrease with altitude in the upper most part of our observations for T < 245 K (Fig. 13h). Mie effects of the larger particles are visible for D_{max} > 2 mm and are most pronounced in the levels from 260–275 K.

ACPD
14, 2983–3041, 2014

Basically cloud radar reflectivity is strongly correlated with the mass concentrations of ice (e.g., Hogan et al., 2006; Protat et al., 2007). Figure 13 shows Z–CWC relationships derived from MT2010, MT2011, and the merged dataset of both campaigns. Since the $m(D)$ coefficients have been constrained by the RASTA radar reflectivity it is not surprising to find a rather good correlation between CWC and the measured RASTA radar reflectivity. Figure 13a–c also depicts the probability density functions (see PDF color scale in Fig. 14) of the partitioning of mass concentrations CWC (α_σ,β_σ) as a function of the radar reflectivity at 94 GHz. During MT2010 (Fig. 13a) the measured reflectivities are essentially found in the range from 10 to 20 dBZ, yielding CWC from 0.3 to 4 g m^{-3}. For MT2011, (Fig. 13b) a significant part of the reflectivity values is found between 5 and 20 dBZ, which corresponds to a mass concentration of CWC in the range of 0.1–2 g m^{-3}. The two Megha-Tropiques campaigns (MT2010 and MT2011) are merged in Fig. 13c.

Z–CWC relationship are fitted as power laws (Eq. 15a–c), with Z in mm^6 m^{-3} and CWC in g m^{-3}. In Fig. 13a–c, Z is expressed in dBZ for convenience.

$$\mathrm{CWC}(Z) = 0.0858Z^{0.759} \quad \text{MT2010} \tag{15a}$$

$$\mathrm{CWC}(Z) = 0.0761Z^{0.715} \quad \text{MT2011} \tag{15b}$$

$$\mathrm{CWC}(Z) = 0.0783Z^{0.768} \quad \text{MT2010 + MT2011} \tag{15c}$$

Pre-factors of these three power laws give CWC values at 0 dBZ (1 mm^6 m^{-3}), namely 0.085 g m^{-3} for MT2010 and 0.076 g m^{-3} for MT2011. This leads to a difference of about 0.009 g m^{-3} (although at low CWC values) between the 2 campaigns for one and the same reflectivity.

Relative errors in the retrieved CWC, by using the Z–CWC fit (error$_Z$), with respect to the values of CWC(α_σ,β_σ) are calculated in the following way (Eq. 16):

$$\mathrm{error}_Z = 100\frac{|\mathrm{CWC}(Z) - \mathrm{CWC}(\alpha_\sigma,\beta_\sigma)|}{\mathrm{CWC}(\alpha_\sigma,\beta_\sigma)}. \tag{16}$$

ACPD
14, 2983–3041, 2014

For MT2010 (Table 5) the majority of error$_Z$ values are below 53 % (90th percentile), with a mean error$_Z$ of about 28 %. For MT2011 the mean errorz is about 41 % with a majority of error$_Z$ below 48 %. The mean error$_Z$ for the merged dataset (MT2010 and MT2011) is 35 % and the majority of the error$_Z$ are below 68 %.

Results of an inter comparison between the three Z–CWC relationships deduced for the Megha-Tropiques data (MT2010, MT2011, MT2010+MT2011) and two further relationships given by Protat and al. (2007), hereafter denoted P2007 are shown in Fig. 14. Relationships given by P2007 are based on cloud in-situ observations using a tropical dataset (Eq. 17a) and from a global dataset (Eq. 17b) which includes also mid-latitude and tropical clouds. Note that the BF95 $m(D)$ relationship has been assumed for all clouds in their calculations.

$$\mathrm{CWC}(Z) = 0.149 Z^{0.681} \quad \text{Global P2007} \tag{17a}$$

$$\mathrm{CWC}(Z) = 0.198 Z^{0.701} \quad \text{Tropics P2007} \tag{17b}$$

Applying P2007 parameterizations for calculating CWC, results in significantly larger CWC values, as compared to estimated CWC of this study for the Megha-Tropiques dataset, which is particularly true for small reflectivities. Differences in CWC calculated from P2007 and estimated from this study reach up to a factor of 4 for lowest reflectivities. This might be due to the fact that the in-situ database used in P2007 encompasses a much larger variety of ice clouds, including low CWC cirrus clouds. However, it also probably indicates (as was also highlighted in Protat and Williams, 2011) that the use of a single $m(D)$ relationship for all clouds is not appropriate because it excludes the large natural variability of $m(D)$ in these Z–CWC relationships.

The curves for MT2010 and MT2011 only differ for reflectivities above 5–10 dBZ. Below 0 dBZ, Z–CWC relationships of MT2010 and MT2011 are close. The difference occurring for the larger reflectivities may due to the presences of higher CWC accompanied by larger ice particles and stronger number concentrations encountered during MT2010 (see Figs. 11 and 12). In fact about 70 % of RASTA reflectivities measured during MT2010 are larger than 10dBZ, while for MT2011 only 40 % of measured val-

ACPD
14, 2983–3041, 2014

ues of RASTA reflectivities are larger than 10 dBZ. The main reason is that for a given reflectivity, different values of CWC are calculated for MT2010 and MT2011, which is highly related to differences in the flattening parameter found for MT2010 and MT2011, respectively. Figure 15 shows the average of the flattening of the hydrometeors as a function of temperature. Overall the main feature is a weak increase of the mean aspect ratio $\overline{As}$ with altitude and a larger value of $\overline{As}$ in the continental clouds relative to oceanic clouds. In addition, the increase in $\overline{As}$ with altitude is larger for continental MCS, thus impacting the Z–CWC relationships.

In the case of small reflectivities < 0–5 dBZ, we can assume that larger ice particles may be less present. The reflectivities of small ice crystals below 800 µm are not influenced by Mie effects and are not a function of the particles' aspect ratio (see Fig. 2). Thus the Z–CWC relationships for MT2010 and MT2011 almost agree for small cloud reflectivity. Finally, the influence of the temperature on the Z–CWC relationships has been studied, however no clear signature has emerged. It seems that using the T-matrix method to simulate the reflectivity of the hydrometeors removes the impact of temperature on the Z–CWC relationship, at least for the stratiform part of tropical MCS.

6 Discussion and conclusion

This study presents a method to calculate the exponent and the pre-factor of the $m(D)$ power law relationship, using 2-D cloud particle imagery (OAP 2-DS and PIP) and measured cloud radar reflectivities at a frequency of 94 GHz. The T-matrix method has been used to simulate the reflectivities of the hydrometeors which are represented as oblate spheroids. The method has been applied to two different tropical stratiform anvil datasets, one collected over the African Continent (MT2010) and the other one collected above the Indian Ocean (MT2011). The two campaigns have been compared using the derived parameters of the 2-D imagery in combination with measured radar reflectivities. It is clearly found that the variability of the $m(D)$ coefficients α and β is large, and that these coefficients both decrease with altitude, which implies a decrease

ACPD
14, 2983–3041, 2014

of the density of the larger hydrometeors. The decrease of $m(D)$ coefficients with altitude in the stratiform part of MCS is larger over the ocean than over the continent, reflecting different efficiency of the microphysical processes over land and ocean. On average it has been found that for MT2010 $\alpha = 0.0244$ and $\beta = 2.44$, and for MT2011 $\alpha = 0.0266$ and $\beta = 2.44$, respectively. In contrast, the total crystal number concentration increases with altitude, and the number concentrations are larger over the continent (MT2010) than over the ocean (MT2011).

Furthermore, it has been noticed that the global reflectivity decreases with altitude for both types of MCS. Over the African continent the concentration of hydrometeors larger than 2 mm is rather constant with altitude. Since $\overline{As}$ increases with altitude, the reflectivity of the larger hydrometeors decreases with altitude, thus impacting the reflectivity. For the oceanic MCS the decrease of the concentration of the larger hydrometeors ($D_{max} > 2$ mm) with altitude is accompanied by an increase of the $\overline{As}$, which impacts more the reflectivity at small reflectivity values (~ -5 dBZ) around 240 K. This leads to differences in the retrieved condensed water content at the 240 K level of almost 1 order of magnitude ($\sim 0.8\,g\,m^{-3}$ for MT2010 and $0.1\,g\,m^{-3}$ for MT2011).

Continental MCS in the monsoon seasons are due to the convergence of wet colder air masses from the ocean with dry warmer air masses, while over the Indian Ocean convection is due to the buoyancy of wet air masses leading to weaker convection in our case. Growth processes of hydrometeors in oceanic convection were to a non negligible extent due to vapor diffusion producing many dendrites and plates that have been observed. In contrast, for West-African MCS the hydrometeor growth was much more dominated by riming and aggregation processes, thus leading to observations of aggregates and graupels-like shapes. Figure 16 summarizes the observations of typical crystal morphologies observed during the 2 campaigns. 2-D images are presented as a function of altitude. On the left side of Fig. 16 hydrometeors observed in continental MCS are shown, whereas on the right side hydrometeors observed in oceanic MCS are presented. In the two first levels (-1 and $-5\,^{\circ}C$) hydrometeors are similar with one exception where at $-5\,^{\circ}C$ a dendrite shows up for MT2011. For others levels

ACPD
14, 2983–3041, 2014

ice crystal shapes are in general different. Observations of significant amounts of dendrites (which typically develop due to water vapor diffusion only) occurred in MT2011, while 2-D images for MT2010 generally look more like aggregates and graupels. These differences are also underlined by a flattening of the hydrometeors which is smaller for oceanic MCS as compared to West-African MCS.

Despite having a large variability of $m(D)$ coefficients for one and the same altitude level and despite having found significant variability of these coefficients with altitude, the differences between continental and oceanic MCS may be significantly related to the number of hydrometeors and also to the shape of the PSD. It appears that the higher the number concentration of hydrometeors, the more dominant the aggregation process. In contrast, when the number of hydrometeors is small the ice crystals grow essentially by vapor diffusion.

Within this study, $m(D)$ power law coefficients were calculated from an indirect method, using particle images and their associated reflectivity signatures. The $m(D)$ retrieval and subsequent CWC calculation have been constrained by the 2-D images. On the one hand, the exponent β of the $m(D)$ relationship is calculated from the relations between maximum lengths and projected surfaces of the hydrometeors. This relation was established for simple but realistic hydrometeor shapes which could be refined with more sophisticated simulations of aggregates of dendrites or more complex shapes. On the other hand, the choice of the flattening of the oblate spheroid used to simulate the reflectivity at 94 GHz is determined by the mean aspect ratio of the hydrometeors recorded within individual time steps of 5 s. As a perspective and without making the simulations of the cloud reflectivities too complex, the parameterizations of the flattening might be further improved as a function of the maximum length of the spheroids used in the T-matrix method. In a near future we will also include as an additional constraint the surface roughness of the hydrometeors which might be a quite important parameter to describe the backscattering properties of the hydrometeors.

ACPD
14, 2983–3041, 2014

Appendix A

Description of 3-D simulations

Simulations of 3-D particle habits have been performed with the overall objective to study the $S(D)$ and $m(D)$ relations including correlations between the two exponents of the power laws. The simulated shapes aim to be realistic or at least comparable to the variety of hydrometeors found in natural clouds. All crystal shapes considered have 3-D characteristics with known volume or mass and for the simulation they are randomly oriented in the 3-D space.

A1 Plates

The schematic of a plate type crystal is presented in Fig. A1. The geometric parameters used are the thickness H and the height L between 2 opposed corners of the hexagon. The simulations distinguish four types of plates, in order to explore the influence of the ratio between H and L on the fitted power laws. Two simulations have a ratio of H/L equal to 0.1 and 0.2, whereas in the third simulation H is equal to the square root of L and in the fourth H is constant and equal to 4 pixels. In all these simulations, L is chosen randomly out of the interval from 20 to 200 pixels with 1000 thousands simulations of plates in each of the four cases.

A2 Columns

Figure A2, shows the principal schematic of a column with geometric parameters of height H and thickness L between 2 corners of the hexagon. As has been performed for the plates, four sets of simulations were performed for columns: two with a linear ratio between H and L, with H/L equal to 10 and 5, whereas in the third simulation L is equal to the square root of H and in the fourth L is constant and equal to 16 pixels.

ACPD
14, 2983–3041, 2014

L has been chosen out of the size range of [10;100] pixels with 1000 simulations for columns in each of the four cases.

A3 Slender stellars and more solid stellars

Two types of stellar crystals were simulated with a significant difference in the width of their branches (Fig. A3). We call these two types slender stellars (lower picture) and solid stellars (upper picture). For both types of stellars, four sets of 1000 simulations were performed. Two simulations have a ratio of H/L equal to 0.1 and 0.2, whereas in the third simulation H is equal to the square root of L and in the fourth H is constant and equal to 4 pixels.

A4 Aggregates of spheres

Another type of crystals has been simulated, which subsequently is called aggregates of spheres, see Fig. A4. N is the random number of spheres, ranging between 3 and 50, which are aggregated, and D is the diameter of one sphere which is set constant and equal to 6 pixels. In total 1000 simulations of aggregated spheres were performed.

A5 Capped columns

One type of capped columns was simulated and processed, where the column is capped by two plates. The schematic description of a capped column is shown in Fig. A5. L_1 is the height of the two plates (and large stellars) at the top of the column, L_2 ($= 2.5L_1$) is the thickness of the column, and H ($= L_1$) is its height. For the two simulations L_1 varied between 10 and 100 pixels and the width of the plates (or stellars) has been set to 4 pixels. In total 1000 simulations of capped columns were performed.

ACPD
14, 2983–3041, 2014

A6 Rosettes

A rosette with six branches randomly oriented is shown in Fig. A6. To simplify the scheme of the bullets that constitute the rosette, the bullets are assimilated as hexagonal columns. All the bullets belonging to the same rosette have identical size parameters, where H is the bullet's height, L its thickness, and N the maximum number of bullets building the rosette.

In total, nine series of simulations were performed, varying N between 3 and 6 bullets. Three simulation series have been performed with N equal to 3 and where the bullets are described either by L equal to the square root of H or L equal to 5 pixels, or by the ratio L/H equal to 0.25. H has been chosen out of the size range of 5 to 50 pixels.

Two sets of simulations followed where N is equal to 4 and where the bullets are described by L equal to the square root of H, or L equal to 10 pixels. H has been chosen out of the size range of 10 to 100 pixels.

Two further sets of simulations were performed where N is equal to 5 and where the bullets are described by L equal to 10 pixels, or by the ratio L/H equal to 0.2. H has been chosen out of the size range of 10 to 100 pixels.

Finally, two additional sets of simulations were performed where N is equal to 6 and where the bullets are described as L is equal to the square root of H, or by L equal to 10 pixels. H has been chosen out of the size range of 10 to 100 pixels. All series were studied with 1000 simulations of rosettes.

Acknowledgements. The authors are particularly grateful to CNES for funding the aircraft measurement campaigns within the Megha-Tropiques project. We would like to thank SAFIRE for operating the French Falcon 20 research aircraft during the two campaigns.

ACPD
14, 2983–3041, 2014

References

Baker, B. and Lawson, R. P.: Improvement in determination of ice water content from two-dimensional particle imagery, Part 1: Image-to-mass relationships, J. Appl. Meteorol. Clim., 45, 1282–1290, doi:10.1175/JAM2398.1, 2006.

Baumgardner, D. and Korolev, A.: Airspeed corrections for optical array probe sample volumes, J. Atmos. Ocean. Tech., 14, 1224–1229, doi:10.1175/1520-0426(1997)014<1224:ACFOAP>2.0.CO;2, 1997.

Brown, P. R. A. and Francis, P. N.: Improved measurements of the ice water content in cirrus using a total-water probe, J. Atmos. Ocean. Tech., 12, 410–414, doi:10.1175/1520-0426(1995)012<0410:IMOTIW>2.0.CO;2, 1995.

Field, P. R., Heymsfield, A. J., and Bansemer, A.: Shattering and particle interarrival times measured by optical array probes in ice clouds, J. Atmos. Ocean. Tech., 23, 1357–1371, doi:10.1175/JTECH1922.1, 2006.

Heymsfield, A. J. and Parrish, J. L.: A computational technique for increasing the effective sampling volume of the PMS two-dimensional particle size spectrometer, J. Appl. Meteorol., 17, 1566–1572, doi:10.1175/1520-0450(1978)017<1566:ACTFIT>2.0.CO;2, 1978.

Heymsfield, A. J. and Westbrook, C. D.: Advances in the estimation of ice particle fall speeds using laboratory and field measurements, J. Atmos. Sci., 67, 2469–2482, doi:10.1175/2010JAS3379.1, 2010.

Heymsfield, A. J., Lewis, S., Bansemer, A., Iaquinta, J., Miloshevich, L. M., Kajikawa, M., Twohy, C., and Poellot, M. R.: A general approach for deriving the properties of cirrus and stratiform ice cloud particles, J. Atmos. Sci., 59, 3–29, doi:10.1175/1520-0469(2002)059<0003:AGAFDT>2.0.CO;2, 2002.

Heymsfield, A. J., Schmitt, C., Bansemer, A., and Twohy, C. H.: Improved representation of ice particle masses based on observations in natural clouds, J. Atmos. Sci., 67, 3303–3318, doi:10.1175/2010JAS3507.1, 2010.

Hogan, R. J., Mittermaier, M. P., and Illingworth, A. J.: The retrieval of ice water content from radar reflectivity factor and temperature and its use in evaluating a mesoscale model, J. Appl. Meteorol. Clim., 45, 301–317, doi:10.1175/JAM2340.1, 2006.

Huffman, G. J., Adler, R. F., Bolvin, D. T., Gu, G., Nelkin, E. J., Bowman, K. P., Hong, Y., Stocker, E. F., and Wolff, D. B.: The TRMM Multisatellite Precipitation Analysis (TMPA): quasi-global,

ACPD
14, 2983–3041, 2014

multiyear, combined-sensor precipitation estimates at fine scales, J. Hydrometeorol., 8, 38–55, doi:10.1175/JHM560.1, 2007.
Korolev, A. V., Strapp, J. W., Isaac, G. A., and Nevzorov, A. N.: The Nevzorov airborne hot-wire LWC–TWC probe: principle of operation and performance characteristics, J. Atmos. Ocean. Tech., 15, 1495–1510, doi:10.1175/1520-0426(1998)015<1495:TNAHWL>2.0.CO;2, 1998.
Locatelli, J. D. and Hobbs, P. V.: Fall speeds and masses of solid precipitation particles, J. Geophys. Res., 79, 2185–2197, doi:10.1029/JC079i015p02185, 1974.
McFarquhar, G. M., Timlin, M. S., Rauber, R. M., Jewett, B. F., Grim, J. A., and Jorgensen, D. P.: Vertical variability of cloud hydrometeors in the stratiform region of mesoscale convective systems and bow echoes, Mon. Weather Rev., 135, 3405–3428, doi:10.1175/MWR3444.1, 2007.
Mishchenko, M. I., Travis, L. D., and Mackowski, D. W.: T-matrix computations of light scattering by nonspherical particles: a review, J. Quant. Spectrosc. Ra., 55, 535–575, doi:10.1016/0022-4073(96)00002-7, 1996.
Mitchell, D. L.: Use of mass- and area-dimensional power laws for determining precipitation particle terminal velocities, J. Atmos. Sci., 53, 1710–1723, doi:10.1175/1520-0469(1996)053<1710:UOMAAD>2.0.CO;2, 1996.
Mitchell, D. L., Zhang, R., and Pitter, R. L.: Mass–dimensional relationships for ice particles and the influence of riming on snowfall rates, J. Appl. Meteorol., 29, 153–163, doi:10.1175/1520-0450(1990)029<0153:MDRFIP>2.0.CO;2, 1990.
Nicholls, S., Leighton, J., and Barker, R.: A new fast response instrument for measuring total water content from aircraft, J. Atmos. Ocean. Tech., 7, 706–718, doi:10.1175/1520-0426(1990)007<0706:ANFRIF>2.0.CO;2, 1990.
Ogren, J. A., Heintzenberg, J., and Charlson, R. J.: In-situ sampling of clouds with a droplet to aerosol converter, Geophys. Res. Lett., 12, 121–124, doi:10.1029/GL012i003p00121, 1985.
Pokharel, B. and Vali, G.: Evaluation of collocated measurements of radar reflectivity and particle sizes in ice clouds, J. Appl. Meteorol. Clim., 50, 2104–2119, doi:10.1175/JAMC-D-10-05010.1, 2011.
Protat, A. and Williams, C. R.: The Accuracy of Radar Estimates of Ice Terminal Fall Speed from Vertically Pointing Doppler Radar Measurements, J. Appl. Meteorol. Climatol., 50, 2120–2138, doi:10.1175/JAMC-D-10-05031.1, 2011.
Protat, A., Delanoë, J., Bouniol, D., Heymsfield, A. J., Bansemer, A., and Brown, P.: Evaluation of ice water content retrievals from cloud radar reflectivity and temperature using

ACPD
14, 2983–3041, 2014

a large airborne in situ microphysical database, J. Appl. Meteorol. Clim., 46, 557–572, doi:10.1175/JAM2488.1, 2007.
Protat, A., Bouniol, D., Delnoë, J., May, P. T., Plana-Fattori, A., Hasson, A., O'Connor, E., Görsdorf, U., and Heymsfield, A. J.: Assessment of cloudsat reflectivity measurements and ice cloud properties using ground-based and airborne cloud radar observations, J. Atmos. Ocean. Tech., 26, 1717–1741, doi:10.1175/2009JTECHA1246.1, 2009.
Schmitt, C. G. and Heymsfield, A. J.: The dimensional characteristics of ice crystal aggregates from fractal geometry, J. Atmos. Sci., 67, 1605–1616, doi:10.1175/2009JAS3187.1, 2010.
Spencer, R. W., Goodman, H. M., and Hood, R. E.: Precipitation retrieval over land and ocean with the SSM/I: identification and characteristics of the scattering signal, J. Atmos. Ocean. Tech., 6, 254–273, doi:10.1175/1520-0426(1989)006<0254:PROLAO>2.0.CO;2, 1989.
Viltard, N., Burlaud, C., and Kummerow, C. D.: Rain retrieval from TMI brightness temperature measurements using a TRMM PR-based database, J. Appl. Meteorol. Clim., 45, 455–466, doi:10.1175/JAM2346.1, 2006.

ACPD
14, 2983–3041, 2014

Table 1. List of Falcon 20 research flights used in this study.

Flight program	Flight number	Day	Hour (UTC)	Cloud type
MT2010 Continental	Flight 15	6 Aug 2010	16:10–19:00	MCS squall line
	Flight 17	10 Aug 2010	08:45–11:60	MCS squall line
	Flight 18	13 Aug 2010	13:20–16:25	MCS squall line
	Flight 19	17 Aug 2010	10:30–13:40	MCS squall line
	Flight 20	17 Aug 2010	23:35–02:40	MCS squall line
MT2011 Oceanic	Flight 45	27 Nov 2011	05:30–08:50	MCS ITCZ
	Flight 46	27 Nov 2011	15:15–18:25	MCS ITCZ
	Flight 49	6 Dec 2011	13:25–15:40	Isolated Convective System
	Flight 50	8 Dec 2011	06:00–09:00	Isolated Convective System

ACPD
14, 2983–3041, 2014

Table 2. Uncertainty of retrieved CWC and α as a function of the uncertainty of the measured reflectivity.

ΔZ [dBZ]	$\Delta\alpha$ (%)	ΔCWC (%)
−2	+26	−26
−1	+12	−12
+1	−11	+11
+2	−21	+21

ACPD
14, 2983–3041, 2014

Table 3. Uncertainty of retrieved CWC and α as a function of the uncertainty on the average aspect ratio of 2-D images.

$\Delta\overline{As}$ (%)	$\Delta\alpha$ (%)	ΔCWC (%)
−20	+12	−12
−10	+6	−6
+10	−6	+6
+20	−13	+13

ACPD
14, 2983–3041, 2014

Table 4. Ice crystal types and corresponding exponents (σ) and (β) of $S(D)$ and $m(D)$ relations, respectively. The symbols in the left column are subsequently used in Fig. 7 for individual ice crystal shapes. The first part of the table stems from Mitchell (1996) where random orientation is assumed for particles with $D_{max} < 100\,\mu m$, whereas for particles beyond 100 µm horizontal orientation is assumed. The second part of the table stems from simulations.

Symbol	Description	Range	σ	β
	Ice crystal shapes from Mitchell (1996)			
	hexagonal plates	$15\,\mu m < D_{max} < 100\,\mu m$	1.85	2.45
	hexagonal plates	$100 < D_{max} < 3000\,\mu m$	2	2.45
	hexagonal columns	$30 < D_{max} < 100\,\mu m$	2	2.91
	hexagonal columns	$100 < D_{max} < 300\,\mu m$	1.5	1.91
	hexagonal columns	$D_{max} > 300\,\mu m$	1.41	1.74
	rimed long columns	$200 < D_{max} < 2400\,\mu m$	1.41	1.8
	crystals with sector-like branches (P1b)	$10 < D_{max} < 40\,\mu m$	1.85	2.42
	crystals with sector-like branches (P1b)	$40 < D_{max} < 2000\,\mu m$	1.97	2.02
	broad-branched crystals (Plc)	$10 < D_{max} < 100\,\mu m$	1.85	2.42
	broad-branched crystals (Plc)	$100 < D_{max} < 1000\,\mu m$	1.76	1.8
	stellar crystals with broad arms (P1d)	$10 < D_{max} < 90\,\mu m$	1.85	2.42
	stellar crystals with broad arms (P1d)	$90 < D_{max} < 1500\,\mu m$	1.63	1.67
	densely rimed dendrites (R2b)	$1800 < D_{max} < 4000\,\mu m$	1.76	2.3
	side planes (S1)	$300 < D_{max} < 2500\,\mu m$	1.88	2.3
	bullet rosettes, 5 branches at −42 °C	$200 < D_{max} < 1000\,\mu m$	1.57	2.26
	aggregates of side planes	$600 < D_{max} < 4100\,\mu m$	1.88	2.2
	aggregates of side planes, columns & bullets (S3)	$800 < D_{max} < 4500\,\mu m$	1.88	2.1
	assemblies of planar poly-crystals in cirrus clouds	$20 < D_{max} < 450\,\mu m$	1.88	2.45
	lump graupel (R4b)	$500 < D_{max} < 3000\,\mu m$	2	2.8
	hail	$5000 < D_{max} < 25\,000\,\mu m$	2	3

ACPD
14, 2983–3041, 2014

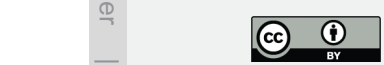

Table 4. Continued.

Symbol	Description	Range	σ	β
	Simulations of ice-crystals shape			
	plates ($H = 0.2 \cdot L$)	$200 < D_{max} < 2000\,\mu m$	2.00	2.98
	plates ($H = 0.1 \cdot L$)	$200 < D_{max} < 2000\,\mu m$	2.00	2.94
	plates ($H = 40\,\mu m$)	$200 < D_{max} < 2000\,\mu m$	1.86	2.02
	plates ($H = \sqrt{L}$)	$200 < D_{max} < 2000\,\mu m$	1.80	2.49
	columns ($H = 5 \cdot L$)	$100 < D_{max} < 1000\,\mu m$	1.93	2.70
	columns ($H = 10 \cdot L$)	$100 < D_{max} < 1000\,\mu m$	1.85	2.46
	columns ($L = \sqrt{H}$)	$100 < D_{max} < 1000\,\mu m$	1.49	1.75
	columns ($L = 160\,\mu m$)	$100 < D_{max} < 1000\,\mu m$	1.06	0.94
	thick star ($H = 0.2 \cdot L$)	$200 < D_{max} < 1200\,\mu m$	1.98	2.90
	thick star ($H = 0.1 \cdot L$)	$200 < D_{max} < 1200\,\mu m$	1.95	2.87
	thick stars ($H = \sqrt{L}$)	$200 < D_{max} < 1200\,\mu m$	1.73	2.48
	thick stars ($H = 40\,\mu m$)	$200 < D_{max} < 1200\,\mu m$	1.61	2.03
	thin Stars ($H = 0.2 \cdot L$)	$100 < D_{max} < 1000\,\mu m$	1.95	2.85
	thin Stars ($H = 0.1 \cdot L$)	$100 < D_{max} < 1000\,\mu m$	1.93	2.81
	thin Stars ($H = \sqrt{L}$)	$100 < D_{max} < 1000\,\mu m$	1.71	2.49
	Thin Stars ($H = 40\,\mu m$)	$100 < D_{max} < 1000\,\mu m$	1.48	2.07
	Aggregates of spheres ($D = 60$; $3 < N < 50$)	$100 < D_{max} < 1000\,\mu m$	1.46	1.64
	Capped columns (2 plates: $L_2 = 2.5L_1$; $H = L_1$)	$150 < D_{max} < 1400\,\mu m$	1.91	2.55
	Rosettes ($L = \sqrt{H}$; $N_{max} = 3$)	$50 < D_{max} < 500\,\mu m$	1.69	2.17
	Rosettes ($L = 50\,\mu m$; $N_{max} = 3$)	$50 < D_{max} < 500\,\mu m$	1.19	0.95
	Rosettes ($L = 0.25 \cdot H$; $N_{max} = 3$)	$50 < D_{max} < 1000\,\mu m$	1.94	2.89
	Rosettes ($L = 100\,\mu m$; $N_{max} = 4$)	$100 < D_{max} < 1000\,\mu m$	1.25	1.14
	Rosettes ($L = \sqrt{H}$; $N_{max} = 4$)	$100 < D_{max} < 1000\,\mu m$	1.67	2.16
	Rosettes ($L = 0.2H$; $N_{max} = 5$)	$500 < D_{max} < 2000\,\mu m$	1.98	2.97
	Rosettes ($L = 100\,\mu m$; $N_{max} = 5$)	$500 < D_{max} < 2500\,\mu m$	1.26	1.16
	Rosettes ($L = 100\,\mu m$; $N_{max} = 6$)	$100 < D_{max} < 1000\,\mu m$	1.28	1.16
	Rosettes ($L = \sqrt{H}$; $N_{max} = 6$)	$100 < D_{max} < 1000\,\mu m$	1.72	2.26

ACPD
14, 2983–3041, 2014

Table 5. Average and 90th percentile of error$_Z$ (in percent) as a function of Z–CWC relationships deduced for the Megha-Tropiques data.

error$_Z$	MT2010	MT2011	MT2010+MT2011
Average	28 %	41 %	35 %
90th percentile	53 %	48 %	68 %

ACPD
14, 2983–3041, 2014

Table A1. List of symbols.

2-DS	2-D stereographic optical array probe with a resolution of 10 µm bin^{-1}
2-DC	2-D cloud particle optical array probe with a resolution of 25 µm bin^{-1}
2-DP	2-D precipitation particle optical array probe with a resolution of 200 µm bin^{-1}
α_i	Vector of prefactor of mass–diameter relationship
α_σ	Prefactor of mass–diameter relationship deduced by the area–diameter relationship and the radar reflectivity
β_i	Vector of exponent of mass–diameter relationship with $\beta \in [1;3]$
β_σ	Exponent of mass–diameter relationship calculated from Eq. (6)
Ar	Area ratio: projected surface divided by $(\pi/4 \cdot D_{max}^2)$
As	mean aspect ratio for a given D_{max} (= width/D_{max})
$\overline{\text{As}}$	mean aspect ratio of all valid 2-D images recorded during a 5 s time period
BRAIN	Bayesian rain rate retrieval algorithm including neural network
CPI	Cloud particle imager, SPEC, Inc.
CWC	Condensed water content (in general)
$CWC_{B\&L}$	CWC deduced from the Baker and Lawson scheme
$CWC(\alpha_i, \beta_i)$	Vector of CWC
$CWC_{Nevzorov}$	Condensed Water ContentMeasured by the Nevzorov probe
D_{max}	Maximum length of the 2-D images of the hydrometeors
ΔD_{max}	Bin resolution of size distribution in function of D_{max}
D_{Tm}	Diameter of a oblate spheroid used by the T-matrix method
$\overline{CWC(\alpha_i,\beta_i)}$	Mean value of the $CWC(\alpha_i,\beta_i)$
ΔCWC_{max}	Uncertainty on the retrieved CWC from RASTA reflectivity and 2-D imagery of OAP
$error_Z$	Absolute error using Z–CWC power fit and the retrieved CWC
f_{ice}	Ice fraction in the oblate spheroid used fort he calculation of the backscattering properties of the hydrometeors
MADRAS	Microwave analysis & detection of rain & atmospheric systems
$m(D)$	mass–diameter relationship
M	Total mass concentration calculated in function of D_{max} per bin
MT2010	Megha-Tropiques Falcon 20 measurement campaign (Niger, Aug 2010)
MT2011	Megha-Tropiques Falcon 20 measurement campaign (Gan, Nov–Dec 2011)
N_{2DS}	Number concentration of hydrometeors counted by the 2-DS
N_{PIP}	Number concentration of hydrometeors counted by the PIP
N	Number concentration of hydrometeors
N_t	Total number concentration of hydrometeors
OAP	Optical array probe
PIP	Precipitation Imaging Probe
PSD	Particle Size Distribution
RASTA	French acronym for Radar Aéroporté et Sol de Télédétection des propriétés nuAgeuse
ρ_{ice}	Ice density: 0.917 g cm^{-3}
ρ_{eff}	Effective density of an ice sphere with a same mass than an ice hydrometeor with a same diameter D_{max}
$S(D)$	Surface–diameter relationship or area–diameter relationship
Sp	Projected surface of an hydrometeors recorded by an OAP
AsD	Aspect ratio distribution
Q_{back}	Total backscattering coeficient in a cubic meter in function of D_{max} per bin

ACPD
14, 2983–3041, 2014

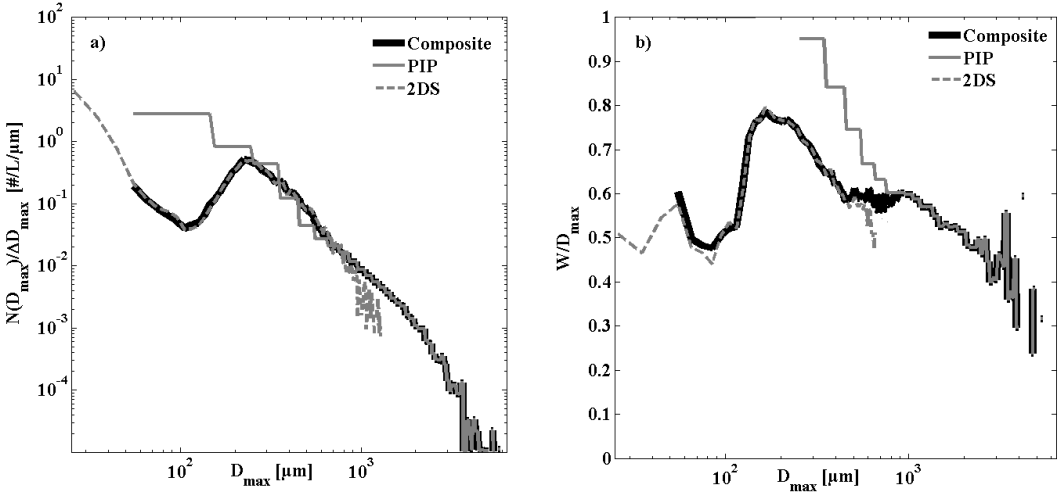

Fig. 1. (a) Number size distributions (as a function of D_{max}) of cloud particles. The dashed grey line represents the 2-DS data, the grey line the PIP data, and the bold black line represents the composite particle number size distribution (PSD). **(b)** Aspect ratio of 2-D particles as a function of D_{max}. Symbols for 2-DS and PIP as above. All curves (number size distributions and aspect ratios) represent an average over 5 s of measurements.

ACPD
14, 2983–3041, 2014

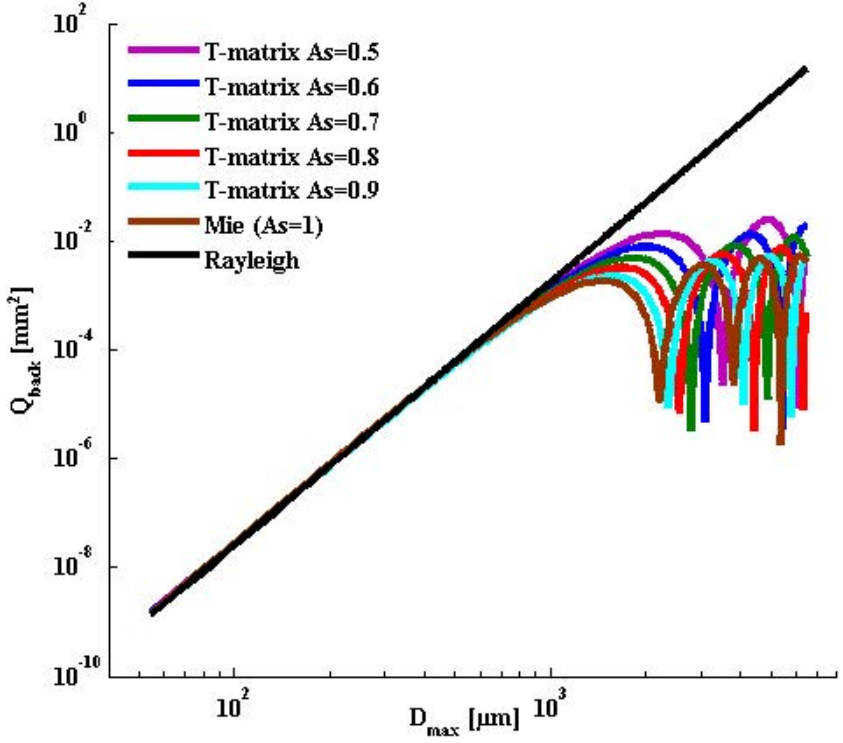

Fig. 2. Calculated effective reflectivity Z_e (in mm^6) as a function of the the maximum particle diameter D_{max} (in µm). Pink, blue, green, red and cyan curves are calculated for different aspect ratios by the T-matrix method, whereas the brown curve is based on Mie theory calculation for a spherical particle. The black curve represents the Rayleigh approximation.

ACPD
14, 2983–3041, 2014

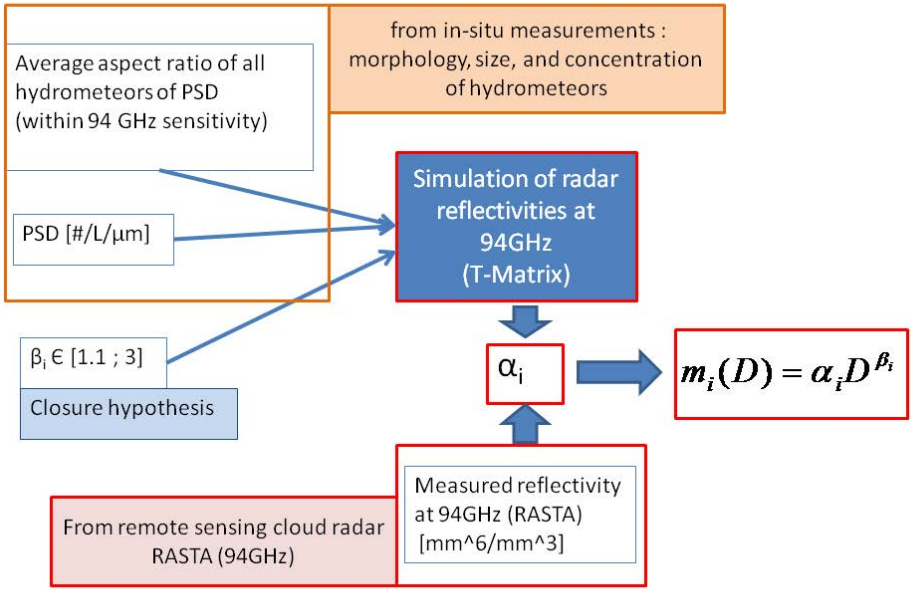

Fig. 3. Implemented method to retrieve the coefficients (pre-factor and exponent) of the mass–diameter relationship from the combination of radar reflectivity and 2-D hydrometeor images. Measured radar reflectivity and hydrometeor particle size distributions and average aspect ratios serve as input for the T-matrix method used for reflectivity simulations for variable β exponents. Closure hypothesis between measured and simulated reflectivities then yield the pre-factor α.

ACPD
14, 2983–3041, 2014

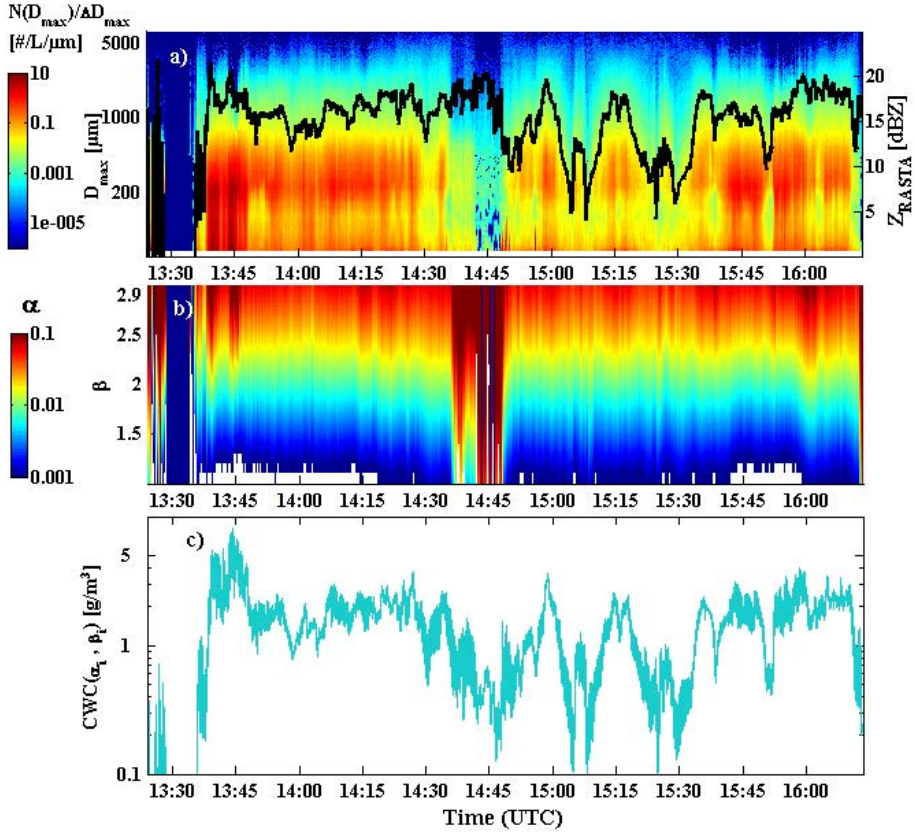

Fig. 4. Flight 18 of MT2010. **(a)** Contour plot of the time series of the number PSD (as a function of D_{max}) color coded with the number concentration in $L^{-1}\,\mu m^{-1}$, the red line shows the simultaneously measured radar reflectivity (secondary y axis). **(b)** Contour plot of solutions for α_i (in color) as a function of β_i (y axis). **(c)** All calculated CWC in $g\,m^{-3}$ for corresponding values of α_i, and β_i.

ACPD
14, 2983–3041, 2014

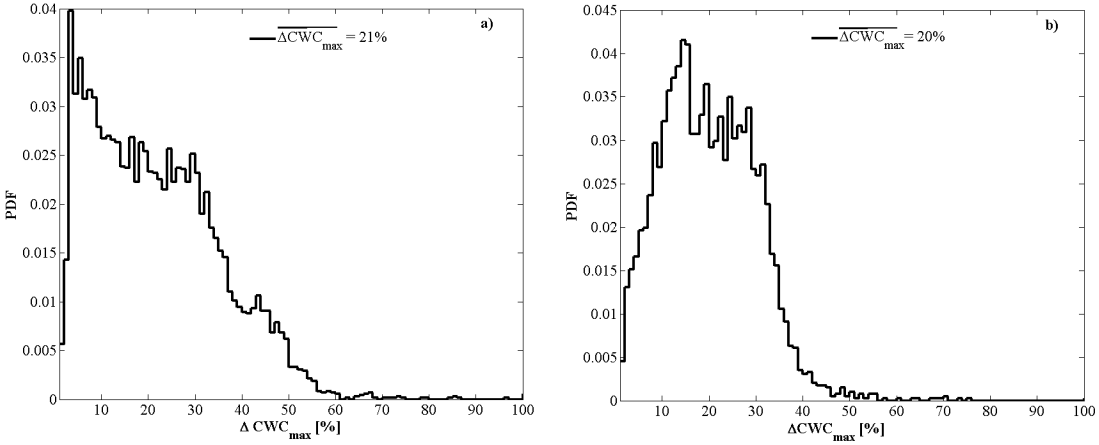

Fig. 5. Histograms of the maximum deviation (ΔCWC_{max}) on the retrieved CWC for **(a)** MT2010 and **(b)** MT2011.

ACPD
14, 2983–3041, 2014

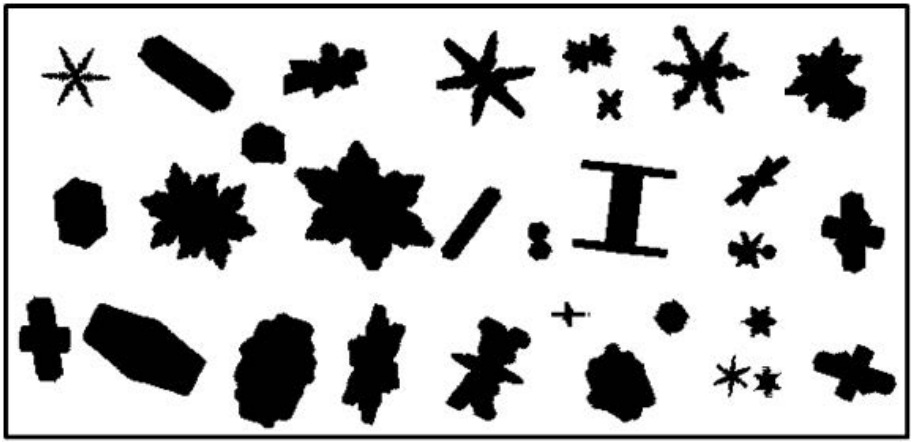

Fig. 6. Examples of projected ice crystals shapes, randomly oriented, in order to simulate the imaging process of 2-D probes.

ACPD
14, 2983–3041, 2014

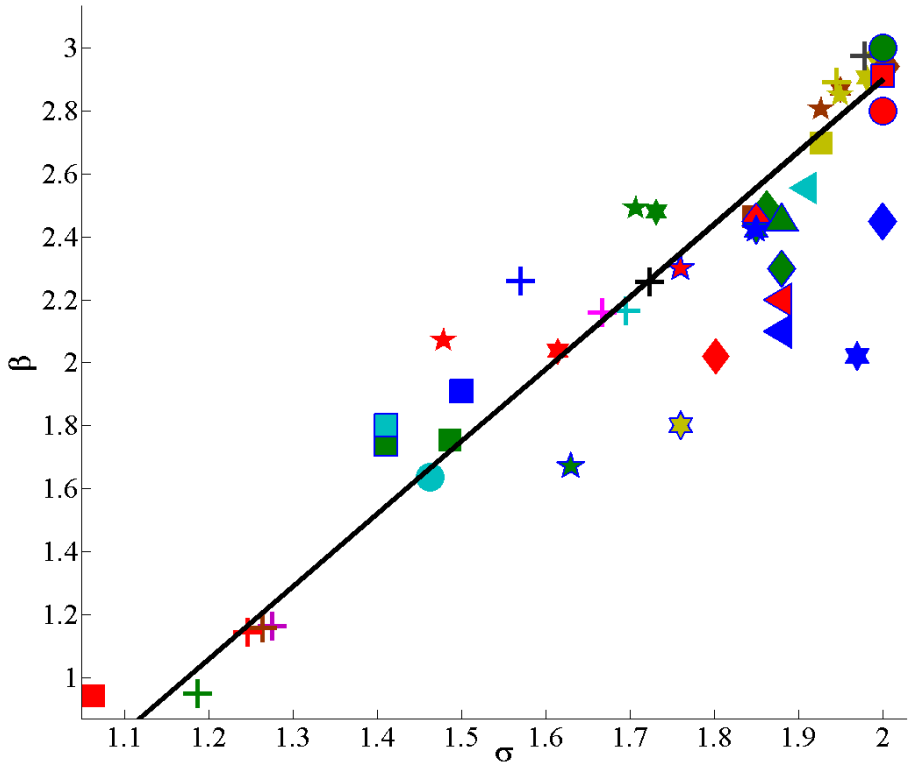

Fig. 7. Exponent β of the $m(D)$ relationship as a function of the exponent σ of the $S(D)$ relationship. Each data point is deduced for a population of 1000 simulated shapes and corresponding projections. Symbols with blue contours stem from Mitchell (1996), whereas all other data points are from 3-D simulations. The legend for all symbols is given in Table 4. A linear fit of all simulated data is shown by the black line.

ACPD
14, 2983–3041, 2014

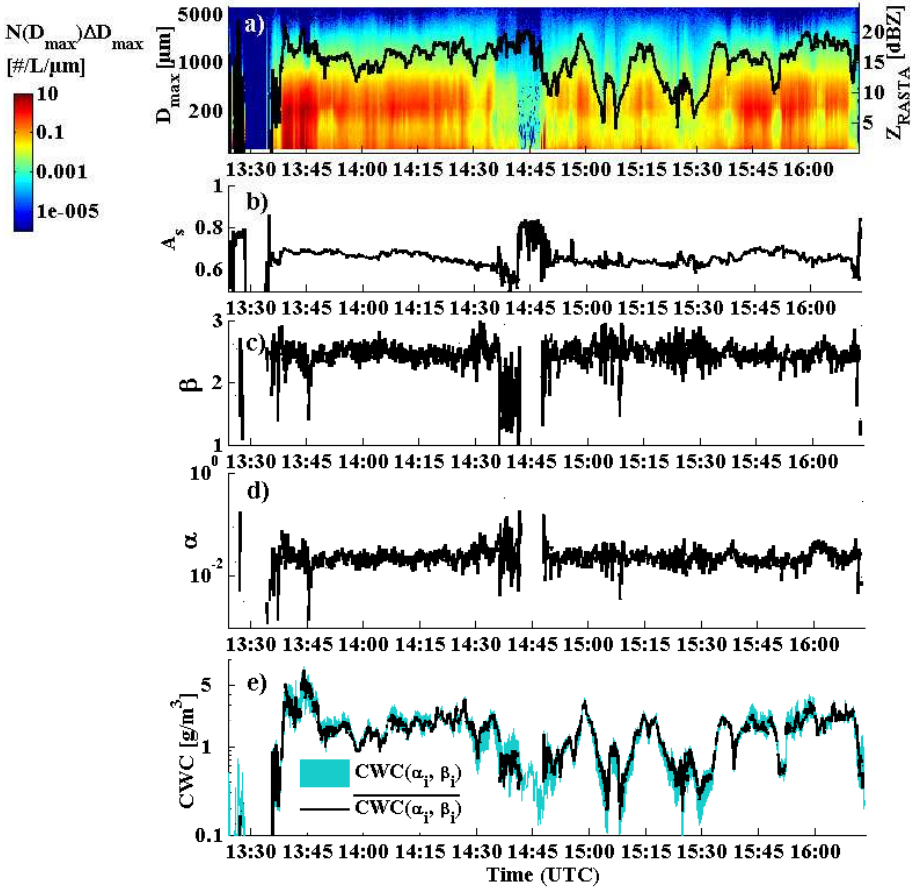

Fig. 8. (a) Same as Fig. 4a. **(b)** Mean aspect ratio along the flight. **(c)** β_σ coefficient calculated from Eq. (12). **(d)** Pre-factor α_σ subsequently deduced from the T-Matrix method. **(e)** All calculated CWC values (blue color) as shown in Fig. 4c, the black line is the CWC deduced from the specific coefficients α_σ and β_σ.

ACPD
14, 2983–3041, 2014

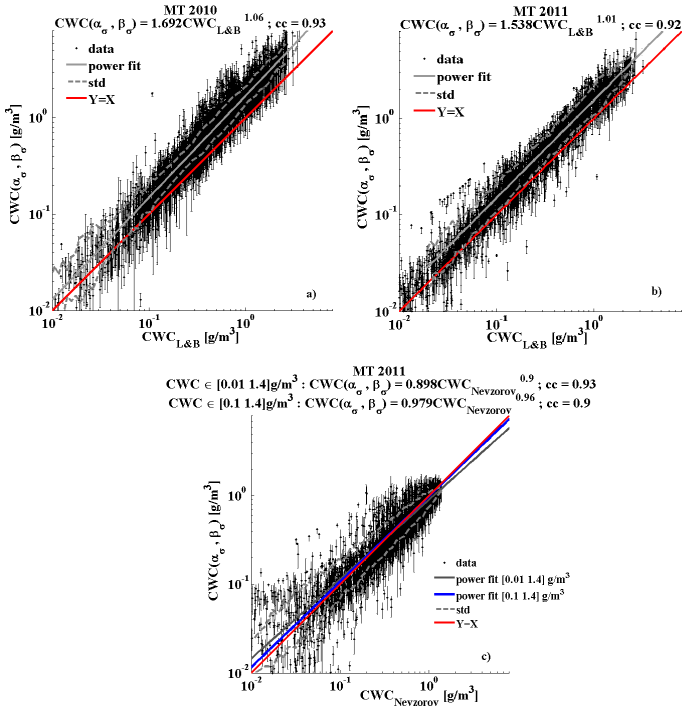

Fig. 9. CWC(α_σ,β_σ) retrieved with T-matrix method (y axis) including error bars vs. CWC (x axis) calculated from Baker and Lawson (2006) for **(a)** MT2010 and **(b)** MT2011. Error bars represent the minimum and the maximum of all possible CWC values (α_i, β_i). The solid grey line represents a power law fit relating the two calculations. The dashed grey lines represent the standard deviation and the red line represents a 1 : 1 relation between CWC (α_σ,β_σ) and CWC from Baker and Lawson (2006). **(c)** CWC from Baker and Lawson (2006) (x axis) is replaced by CWC measured by the Nevzorov probe operated during the MT2011 campaign.

ACPD
14, 2983–3041, 2014

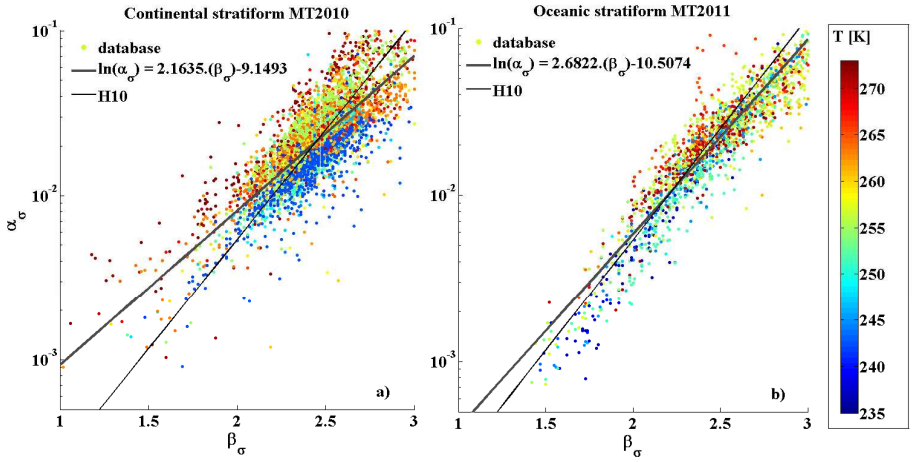

Fig. 10. Scatter plot of exponent β_σ (from Eq. 6) as a function of pre-factor α_σ (constrained by T-Matrix simulations). Data points are color coded as a function of temperature; grey lines represent power law fits. The black lines represent added $m(D)$ power law fits from CRYSTAL-FACE data from H10. **(a)** MT2010 and **(b)** MT2011.

ACPD
14, 2983–3041, 2014

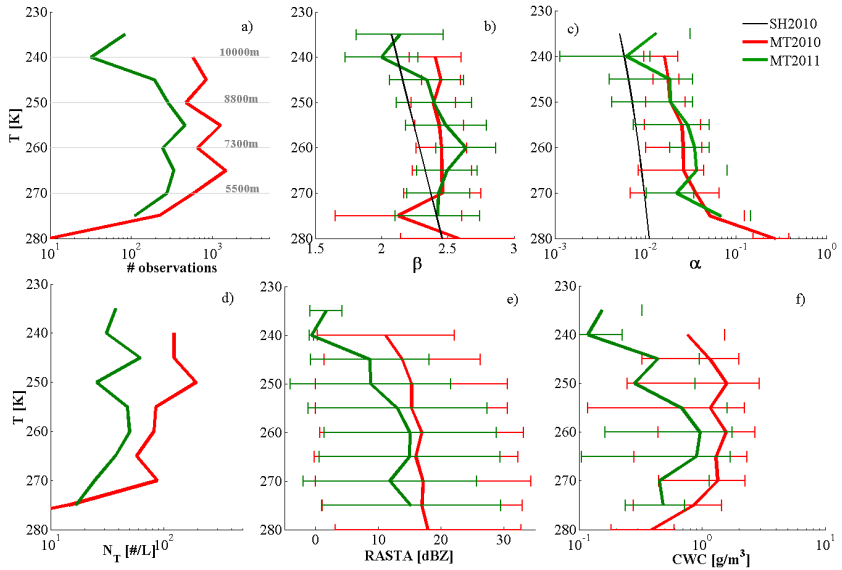

Fig. 11. Vertical profiles of various parameters as a function of temperature (averages for temperature intervals of 5 K): red lines for MT2010, green lines for MT2011, and black lines for SH2010 dataset. **(a)** Number of observations in each temperature interval used for averaging. Altitudes are indicated with horizontal grey lines. **(b)** β_σ coefficient as derived from Eq. (12), the black line represents a fit given by SH2010. **(c)** α_σ coefficient constrained from T-Matrix simulations. **(d)** Total number concentration of hydrometeors. **(e)** RASTA reflectivity, and **(f)** calculated CWC.

ACPD
14, 2983–3041, 2014

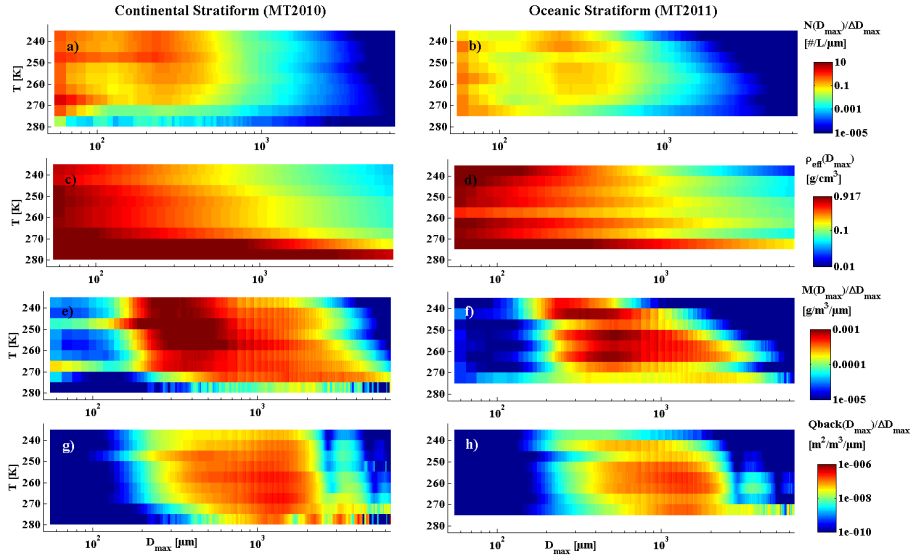

Fig. 12. Contour plots (left MT2010, right MT2011) of average vertical profiles (averages for temperature intervals of 5 K) of microphysical parameters (particle density, total mass and calculated reflectivities at 94 GHz) as a function of D_{max}. **(a–b)** Particles size distribution as a function of D_{max}. **(c–d)** Effective density of a sphere of D_{max} having the same mass as the non-spherical particle. **(e–f)** Total particle mass as a function of D_{max}. **(g–h)** Equivalent reflectivity simulated with the T-matrix method for a frequency of 94 GHz.

ACPD
14, 2983–3041, 2014

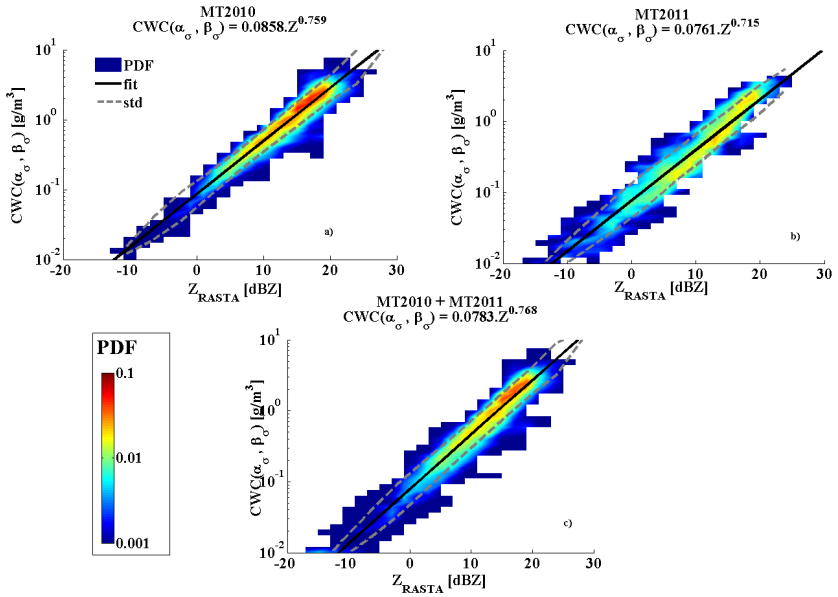

Fig. 13. Normalized probability density function (PDF) of CWC(α_σ,β_σ) as a function of RASTA radar reflectivity. The color code indicates PDF values. Black lines show the power law fits and dashed grey lines the corresponding standard deviations. **(a)** MT2010, **(b)** MT2011, and **(c)** merged MT2010 and MT2011 datasets.

ACPD
14, 2983–3041, 2014

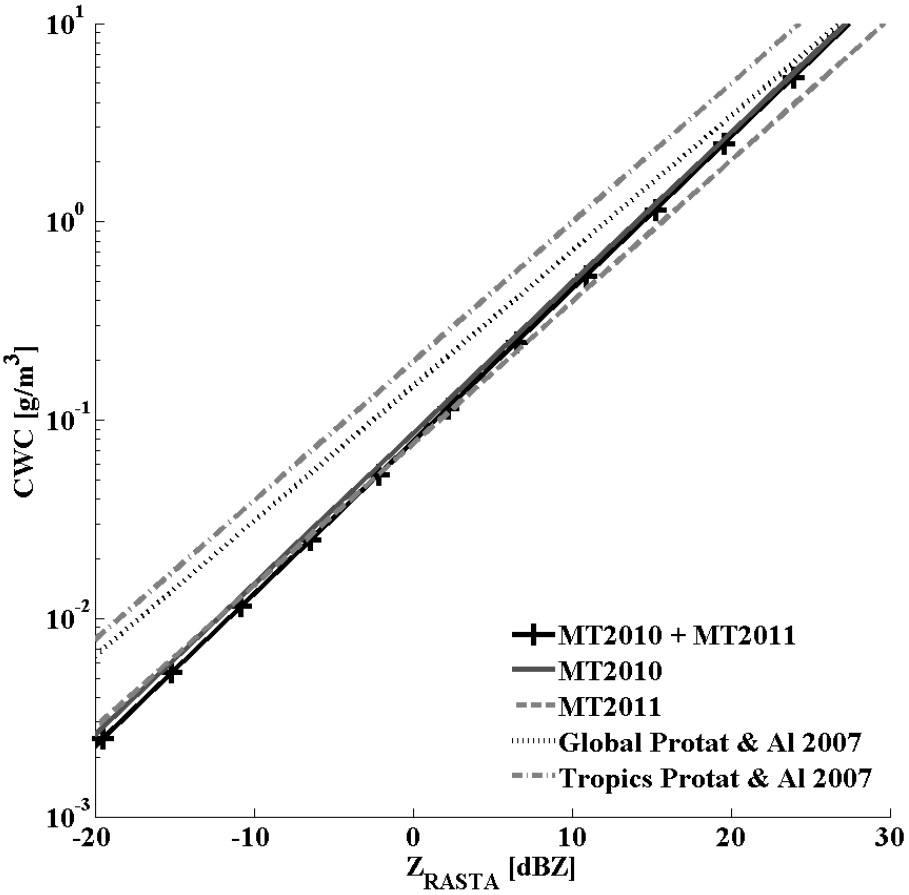

Fig. 14. Z–CWC relationships. Measured RASTA radar reflectivities on the x axis and CWC deduced from the Z–CWC fit for the Megha-Tropiques data. In addition, two further relationships given by Protat et al. (2007) are shown.

ACPD
14, 2983–3041, 2014

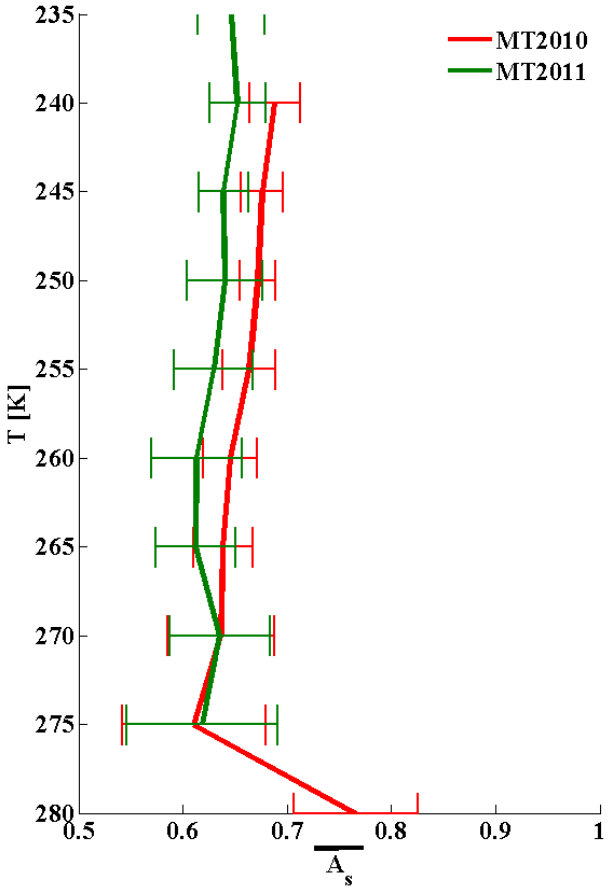

Fig. 15. Averaged aspect ratios plotted as a function of temperature for MT2010 and MT2011.

ACPD
14, 2983–3041, 2014

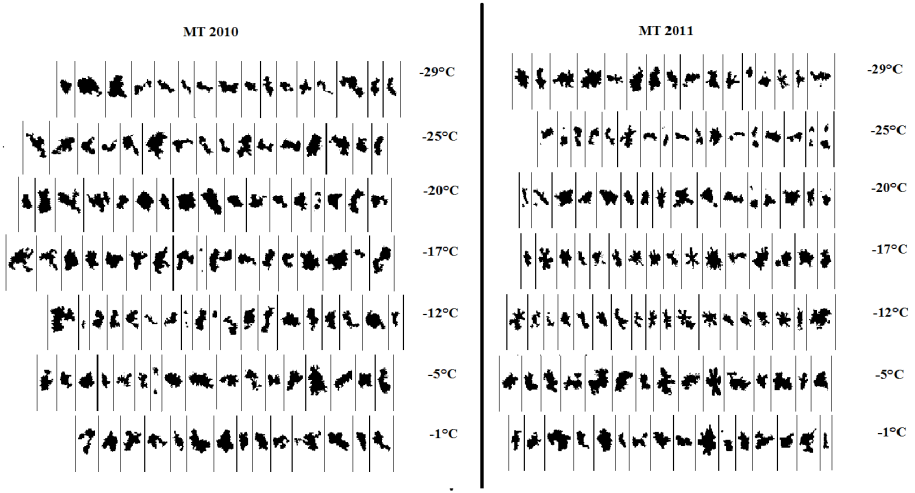

Fig. 16. Examples of 2-D images recorded by the precipitation imaging probe PIP for MT2010 and MT2011. Selected hydrometeor images are presented as a function of temperature in °C and have sizes between 2 to 4 mm. Bars between 2 particles constitute 7 mm.

ACPD
14, 2983–3041, 2014

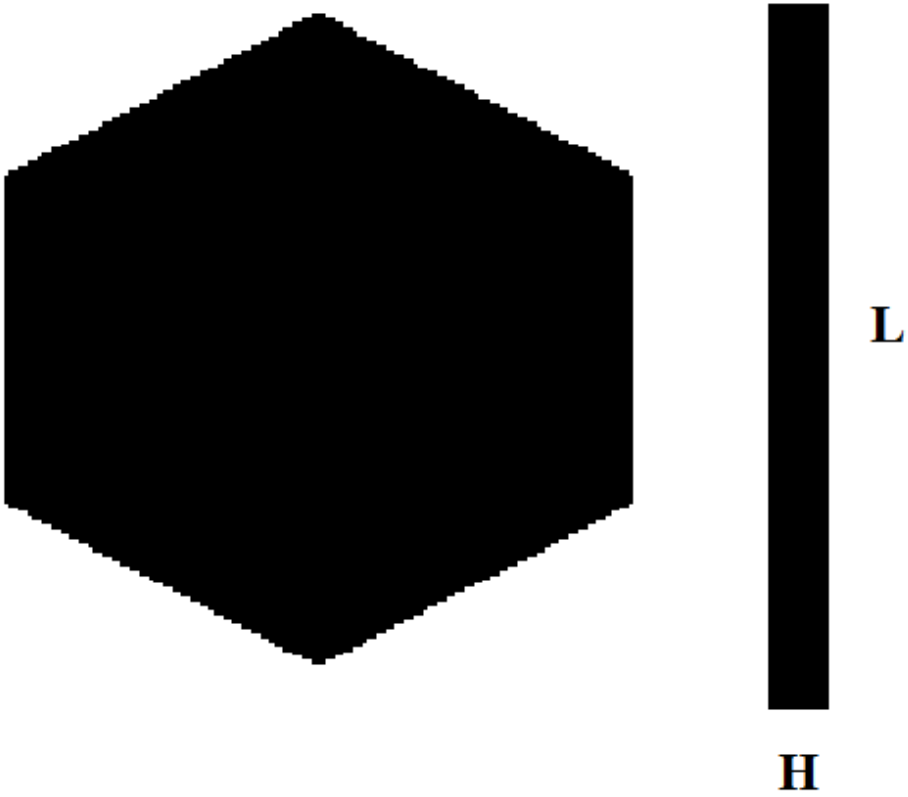

Fig. A1. Schematic description of hydrometeors shapes for subsequent simulations of plate.

ACPD
14, 2983–3041, 2014

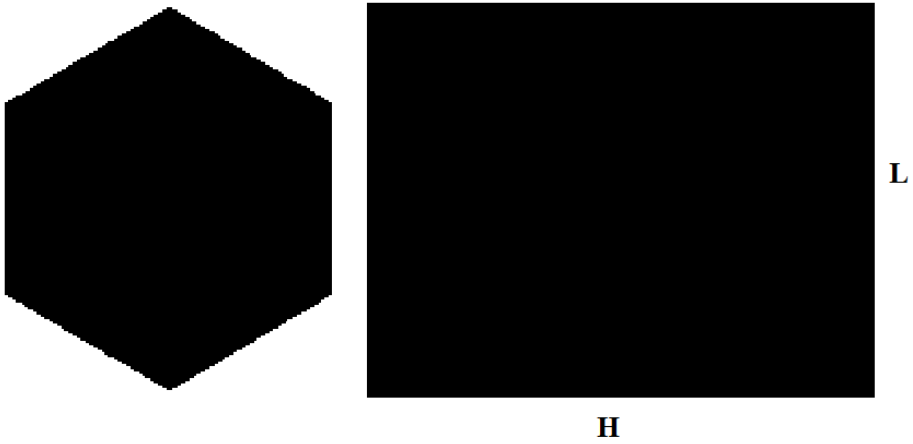

Fig. A2. Schematic description of hydrometeors shapes for subsequent simulations of column.

ACPD
14, 2983–3041, 2014

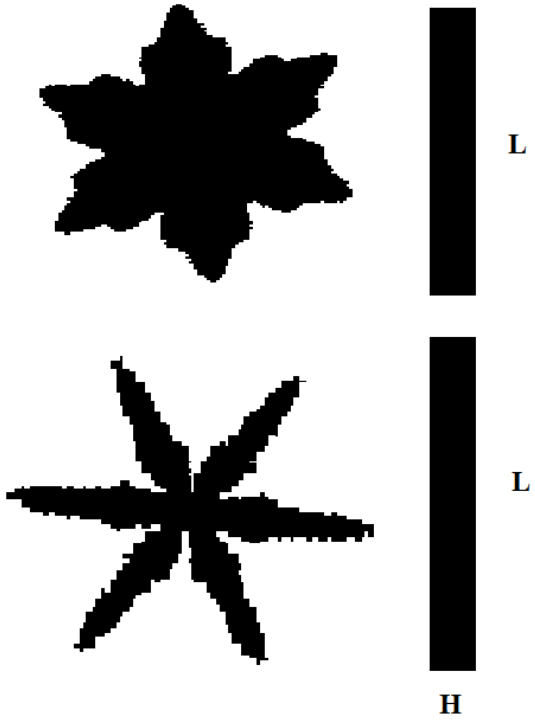

Fig. A3. Schematic description of hydrometeors shapes for subsequent simulations of slender and solid stellar.

ACPD
14, 2983–3041, 2014

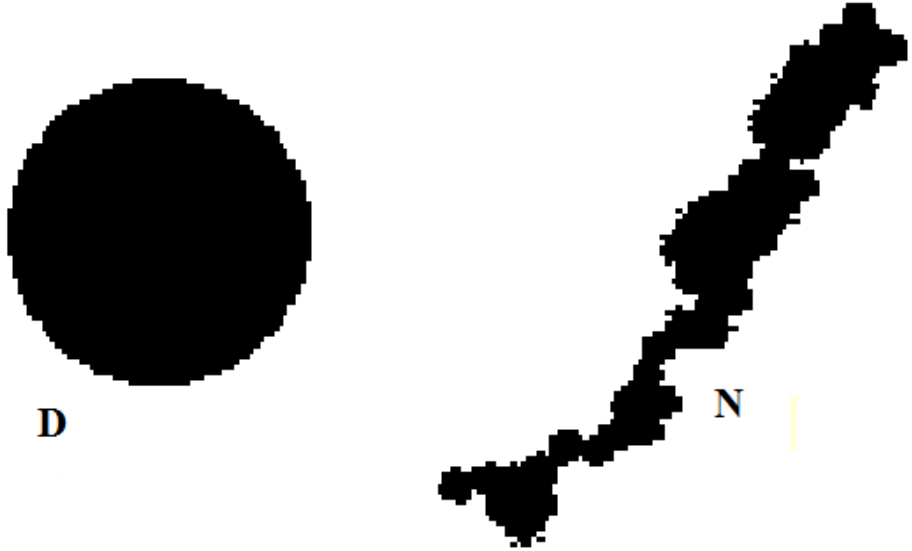

Fig. A4. Schematic description of hydrometeors shapes for subsequent simulations of aggregate of spheres.

ACPD
14, 2983–3041, 2014

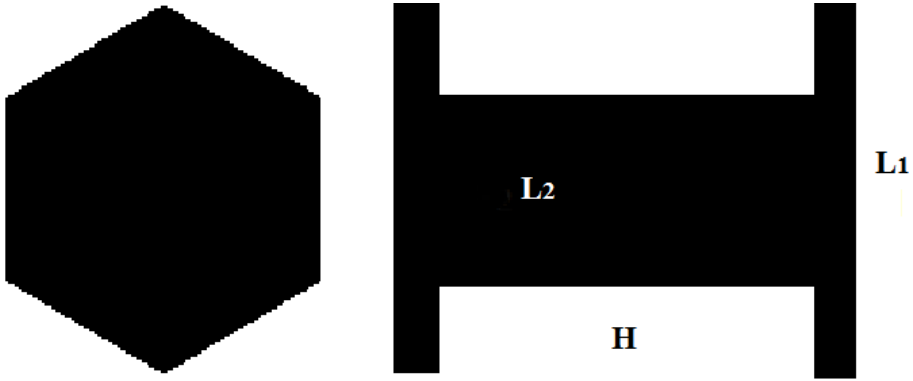

Fig. A5. Schematic description of hydrometeors shapes for subsequent simulations of capped column.

ACPD
14, 2983–3041, 2014

Fig. A6. Schematic description of hydrometeors shapes for subsequent simulations of bullet rosette.

ACPD
14, 2983–3041, 2014